NONADIABATIC MOLECULAR ALIGNMENT MEASUREMENTS VIA PHOTOELECTRON IONIZATION YIELDS AND WHITE-LIGHT GENERATION

A Dissertation

by

GAMZE KAYA

Submitted to the Office of Graduate and Professional Studies of
Texas A&M University
in partial fulfillment of the requirements for the degree of

DOCTOR OF PHILOSOPHY

Chair of Committee,	Hans A. Schuessler
Committee Members,	Rainer J. Fries
	Alvin T. Yeh
	Alexandre A. Kolomenskii
Head of Department,	George R. Welch

December 2015

Major Subject: Applied Physics

ABSTRACT

This dissertation reports a study of nonadiabatic (field-free) molecular alignment for linear molecules. The measurements were performed by measuring photoelectron ionization yields and white-light generation. In the first part of the dissertation, the dynamics of rotational wave packets of the molecules created by a linearly and/or circularly polarized pump pulse were measured by the electron photoionization yields that are produced by a delayed femtosecond probe beam. The photoelectron yields were measured as a function of the linearly polarized probe pulse delay for linearly and/or circularly polarized pump pulses, and revivals of the rotational wave packet were observed in N_2, O_2, CO_2, CO, and C_2H_2 gases. The measured revival structures were compared to the quantum mechanically calculated time dependency of molecular alignment $\langle\langle \cos^2\theta \rangle\rangle$ parameter after the aligning (pump) pulse. The rotational constants of the molecules were also obtained by fitting the theoretically calculated alignment parameter to the measured data. The measured revival structures and rotational constants inferred from the measured data are in good agreement with the calculated results. The second part of the dissertation focuses on evolution of nonadibatic molecular alignment in nitrogen by measuring white-light generation. Again a linearly polarized pump pulse produced a molecular alignment which was measured via its nonlinear interaction effects by a variably delayed filament-producing probe pulse. The induced rotational wave packet was mapped as a function of the angular orientation difference between the polarization directions of the femtosecond pump and probe pulses. The experimental results from mapping rotational wave packets were compared with

quantum mechanically calculated time dependency of molecular alignment $\langle\langle \cos^2\theta \rangle\rangle$ parameter after the pump pulse, which well reproduce all the major observed features.

DEDICATION

To my husband, Necati and to my daughter, Azra

Eşim Necati’ye ve Kızım Azra'ya

ACKNOWLEDGEMENTS

There are many people who have in part helped me through my graduate career here at Texas A&M University and deserve much recognition. I would like to thank my advisor, Dr. Hans A. Schuessler, for providing me with the opportunity to become successful, for sharing with me his knowledge, and for many fruitful and stimulating discussions.

I would like to thank my committee members, Dr. Hans A. Schuessler, Dr. Rainer J. Fries, Dr. Alvin T. Yeh, and Dr. Alexandre A. Kolomenskii, for their guidance and support throughout this research. I would like to thank Dr. Necati Kaya, Dr. James Strohaber, and Dr. Nathan Hart for detailed discussions and assistance related to the research.

I would like to thank all the people in the Attosecond and Few Cycle Laser Laboratory, and my fellow graduate students. Thanks also go to my friends and all other colleagues and the department faculty and staff for making my time at Texas A&M University a great experience.

Last but not least, I am deeply grateful to my parents, Mehmet and Ayse, and my sister, Gulsah, for their great care, support and love. Words cannot express my appreciation and love for my daughter, Azra. Finally, and most importantly, I would like to give my special thanks to Necati for coming into my life and always supporting me in my academic pursuits and for the wonderful life that we share together.

NOMENCLATURE

ATI	above-threshold ionization
θ_l	angle between the molecular axis and polarization direction of linearly polarized light
θ_c	angle between the molecular axis and propagation direction of circularly polarized light
$\hat{J}$	angular momentum operator
M	angular momentum quantum number's projection onto the Z axis
$\Delta\alpha$	anisotropic polarizability of a molecule
P	beam power
ω_0	central angular frequency of the laser
P_{crit}	critical power of self-focusing
$\left\langle \cos^2 \theta_{l,c} \right\rangle$	degree of alignment of a single initial state
$\alpha_{L,C}$	effective polarizability of a molecule for linearly and circularly polarized light
E	electric field
E_0	electric field amplitude
e	electron charge
ρ	electron density
m_e	electron mass
ψ_{el}	electronic wave function

E	energy
Λ_{Gg}	Euler rotation angles for the lab fixed axis G and body fixed axis g
$d_{JM}^{J_0M_0}(t)$	expansion coefficients determined by solving differential equations for linearly or circularly polarized light
H_0	field-free Hamiltonian
FROG	frequency-resolved optical gating
FWHM	full width half max
GRENOUILLE	grating-eliminated no-nonsense observation of ultrafast incident laser light e-fields
H	Hamiltonian
HHG	high harmonic generation
μ	induced dipole moment
J_0	initial rotational state
I	intensity
V_α	interaction potential of the electric field with the induced dipole moment of molecules
V_p	interaction potential of the electric field with the permanent dipole moment of molecules
I_p	ionization potential
P	ionization probability
γ	Keldysh parameter

n_0	linear refractive index
$J_{\max}$	maximum number of excited states
MCP	microchannel plate
MPI	multiphoton ionization
$V_{L,C}$	nonresonant dipole potential
g_{J_0}	nuclear spin factor
ψ_{ns}	nuclear spin wave function
OTBI	over the barrier ionization
I_0	peak intensity
ε_0	permittivity in vacuum
h	Planck's constant
$\alpha_{\|\|}$	polarizability parallel to the molecular axis
$\alpha_{\perp}$	polarizability perpendicular to the molecular axis
U_p	ponderomotive potential
a_0	radius of the beam profile at the 1/e level of intensity
$\hbar$	reduced Planck's constant ($h/2\pi$)
B	rotational constant
J	rotational quantum number
T	rotational temperature
ψ_{rot}	rotational wave function
n_2	second order refractive index
L_{sf}	self-focusing length

c	speed of light in vacuum
$Y_{JM}(\theta,\varphi)$	spherical harmonics
$\left\langle\left\langle \cos^2\theta_{l,c}\right\rangle\right\rangle$	thermally averaged alignment expectation value
$\phi_{J,J'}$	time dependent phase factor associated with $\left\langle\left\langle \cos^2\theta_{l,c}\right\rangle\right\rangle$
TI	tunnel ionization
ψ_{vib}	vibrational wave function
λ	wavelength

TABLE OF CONTENTS

Page

LIST OF FIGURES

Page

LIST OF TABLES

Page

CHAPTER I

INTRODUCTION

1.1 Background

There have been a lot of interest and progress in the general understanding of the interaction of atoms and molecules with intense laser fields (e.g. reviews [1,2]). In modern Ti:sapphire laser systems in 2000s [3-5], femtosecond laser technology has allowed us to observe atomic motion in real time, achieve high harmonic generation, stimulate Raman scattering, as well as obtain the highly nonlinear response of atoms and molecules in strong fields [6,7]. Moreover femtosecond laser technology enables one to align molecules and follow their dynamics by using a pump-probe technique [8]. Studies on molecular alignment and orientation in molecules (see [9,10]) attract considerable interest due to a variety of applications such as controlling chemical reactions [11], producing a selectively-controlled alignment of isotopes [12], imaging of molecular structures [13-15], molecular-frame photoelectron angular distribution [16-18], molecular scattering [19], nanolithography with molecular beams [20], pulse compression [21], and quantum information processing [22]. Moreover, field-free molecular alignment results in a modification of the local optical refractive index, which has been used for controlling the propagation dynamics of weak beams and filaments [23-29].

Aligning creates a dynamically anisotropic medium evolving in time and changing the interaction with laser radiation, which was observed through ionization [30-32],

fragmentation [33-36] and high harmonic generation [13,14,37-44]. Some examples of field-free alignment studies with different detecting methods are presented following.

By using Coulomb explosion measurement technique, Dooley et al. studied rotational wave packet evolution of nitrogen and oxygen molecules by using circularly polarized pulse and they measured two dimensional angular distributions of the wave packet via ion imaging detector [36]. Smeenk and Corkum studied rotational wave packet evolution of oxygen and benzene molecules with circular polarization to observe molecular alignment and created field-free alignment of planar benzene molecules in the polarization plane, a net alignment of linear oxygen molecules outside the polarization plane [45]. Xie et al. demonstrated fragmentation control of acetylene molecule by alignment. They used the molecular alignment to control the yield of molecular fragmentations and accomplished channel selectivity for different fragmentation reactions of acetylene molecule [46].

By using high harmonics of aligned nitrogen molecules, tomographic reconstruction of the highest occupied molecular orbital of nitrogen molecules was demonstrated [13]. Velotta et al. studied molecular orientation dependence of high-order harmonic generation and showed the enhancement of the harmonic intensity of the aligned CS_2, hexane, and N_2 molecules [37]. McFarland et al. studying high harmonic generation of nitrogen molecules observed the first time the influence of electrons occupying the orbital highest occupied molecular orbital-1 which is just below of the highest occupied molecular orbital [44]. Abdurrouf and Faisal demonstrated analytical solutions and compared with the experimental results of aligned nitrogen and oxygen molecules in the

time-domain and in the frequency-domain using high harmonic generation [47]. In other studies, high-order harmonic generation of polyatomic molecules as acetylene and allene was used to show dependence of the harmonic yield on highest occupied molecular orbital symmetry [48], and quantum interference of aligned CO_2 molecules was also obtained in high-order harmonic generation [14,39]. Miyazaki et al. also studied field-free molecular alignment of N_2, O_2, and CO_2 molecules using high-order harmonic generation [49].

Fleischer et al. demonstrated isotope selective molecular alignment of $^{14}N_2$ and $^{15}N_2$ molecules in a nitrogen gas mixture using four wave mixing to observe molecular alignment [12]. Berti et al. numerically studied nonadiabatic laser-induced molecular alignment on the propagation dynamics of a filament [50]. Schippers et al. measured photoacoustically alignment of the linear molecules namely O_2, N_2, CO_2 and CO [51].

Lee et al. showed photoelectron spectra and angular distributions of partially aligned N_2 , O_2 , and CO molecules using low energy above threshold ionization (ATI) of these aligned molecules [52]. Hu et al. studied simulations of the photoelectron spectra displaying ATI peaks of the diatomic O_2 molecule in case of molecular axis is perpendicular to the laser polarization [53]. Smeenk et al. studied photoelectron angular distributions of aligned N_2, O_2, and C_6H_6 molecules from tunnel ionization [54].

Although, commonly the alignment was monitored by the detection of ion yields produced by the probe pulse, in the first part of study, we detected photoelectron from interactions with the probe pulse to directly monitor the alignment process. The dynamics of rotational wave packets in femtosecond laser driven photoelectron ionization yields were studied for laser aligned conjugated linear molecules (N_2, O_2 ,CO_2 CO and C_2H_2).

The measured revival structures are compared to the calculated time dependency of molecular alignment $\langle\langle \cos^2\theta \rangle\rangle$ parameter after the pump pulse. The rotational constants of the molecules were also obtained by fitting the molecular alignment parameter to the time evolution of the measured photoelectron intensity.

In the second part of the study we focus on evolution of nonadibatic molecular alignment in nitrogen by studying white-light generation. The induced rotational wave packet was mapped as a function of the angular orientation difference between the polarization directions of the femtosecond pump and probe pulses. By mapping the ultrafast rotational wave packet (quantum carpet) we demonstrated that the time-dependent phase can be precisely controlled by adjusting the delay of the probe pulse with respect to the pump pulse. The experimental results from mapping rotational wave packets were compared with quantum mechanically calculated time dependency of molecular alignment $\langle\langle \cos^2\theta \rangle\rangle$ parameter after the pump pulse. The good agreement of experimental and simulation results provide a good basis to extend the experimental study to other gases and also have the prospect to be used for more complex systems, such as organic molecules.

1.2 Outline of the dissertation

Chapter II: This chapter covers the theoretical basis of field-free molecular alignment, namely the quantum mechanical approach to describe the interaction of an intense ultrashort pulse with molecules resulting in distinct alignment characteristics.

Chapter III: This chapter gives detailed information about femtosecond laser systems and the pulse measurement techniques that we used.

Chapter IV: In this chapter, starting with background information on the ionization processes, we described our experimental set-up used in this work. A detailed description and results are given on molecular alignment and rotational constants of N_2, O_2, CO_2, CO, and C_2H_2 gases obtained with a linearly and/or circularly polarized pump pulse by measuring photoelectron ionization yields.

Chapter V: This chapter describes the white-light generation and field-free alignment-induced change of the refractive index by a short Gaussian laser pulse in nitrogen gas. The experimental procedure of creating laser-induced rotational wave packets in nitrogen and mapping the induced rotational wave packets as a function of the angular difference between polarization directions of femtosecond pump and probe pulses are described in detail.

Chapter VI: The chapter gives the summary and future perspectives of the research work carried out in the dissertation.

CHAPTER II

THEORY

2.1 Introduction

When a molecule is exposed to a strong laser pulse, this interaction creates an induced dipole moment due to the anisotropic polarizability of the molecule and the molecule tends to align with its most polarizable axis along the laser polarization direction [55]. Based on the comparison between laser pulse duration and rotational revival period of the molecule two different methods are distinguished for the alignment of the molecules called adiabatic alignment and field-free (nonadiabatic or impulsive) alignment. If the laser pulse duration is comparable with the rotational revival period of the molecule "adiabatic alignment" occurs. In this process, the laser field is turned on and off slowly in comparison to the molecular rotational period; the molecules are aligned in the presence of the laser field and then return to the their initial isotropic angular distributions once the laser pulse goes away. If the laser pulse is short (its duration is less than the characteristic molecular rotational time), the scenario is called "nonadiabatic (field-free or impulsive) alignment". The molecules cannot adjust adiabatically to the laser pulse, so this process is called "nonadiabatic alignment". In the nonadiabatic alignment, the short laser pulse creates a rotational wave packet (coherent superposition of the rotational states) in each molecule that will rephrase and dephase in time after the laser pulse has ended. The absence of the aligning laser field after the alignment prevents distortion of the molecular alignment caused by the field, so nonadiabatic alignment has advantageous in comparison with adiabatic alignment to observe molecular dynamics [56-58]. The intensity below the

molecular ionization threshold to observe molecular alignment process is typically order of 10^{12} -10^{13} W/cm^2.

2.2 Theory of nonadibatic molecular alignment

When a linear molecule is subjected to a nonresonant electric field of linearly or circularly polarized light, the molecular axis is spatially confined to the electric field polarization vector. At this point, defining the Z axis is along the electric field polarization vector for linearly polarized light and parallel to the electric field propagation vector for circularly polarized light, alignment between the molecular axis and a space-fixed direction is determined by the expectation value of $\cos^2\theta_{l,c}$ $\left(\left\langle\cos^2\theta_{l,c}\right\rangle\right)$, where $\theta_{l,c}$ is the angle between the molecular axis and the selected axis; l and c indices stand for linearly and circularly polarized light, respectively. This scenario is illustrated in Figure 2.1 (a), where θ_l is the angle between the molecular axis and a Z axis for alignment of a molecule by linearly polarized light and in Figure 2.1 (b) , where θ_c is shown as the angle between molecular axis and the parallel axis to pulse propagation direction Z of the circularly polarized light.

A linear molecule subjected to a nonresonant electric field of linearly or circularly polarized light is experienced a potential due to the interaction of the electric field of the laser and the molecule. The interaction potential $V_{L,C}\left(\theta_{l,c}\right)$ for laser fields defined here as a subscript *L* and *C* for linearly and circularly polarized field, respectively, is given with the expression:

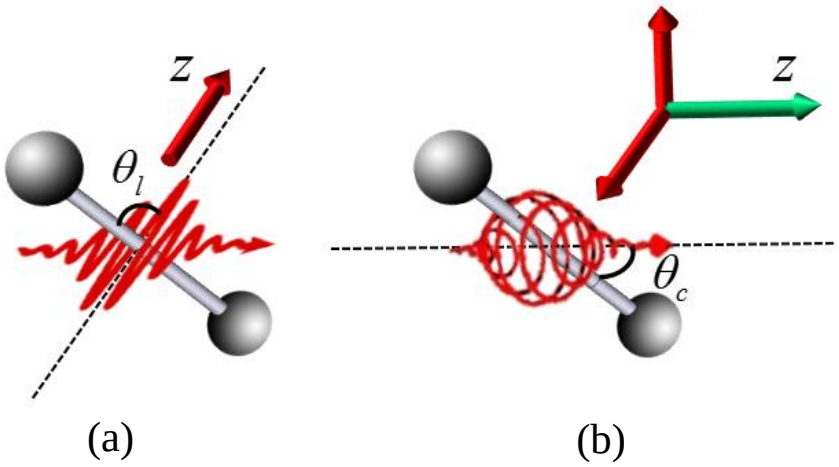

Figure 2.1 The alignment of a diatomic molecule with (a) linearly and (b) circularly polarized light. We choose the Z axis parallel to the electric field vector (red) of linearly polarized light and parallel to the propagation direction (green) of the circularly polarized light, but perpendicular to the plane of the radiation (red).

$$V_{L,C}\left(\theta_{l,c}\right)=V_p\left(\theta_{l,c}\right)+V_\alpha\left(\theta_{l,c}\right) \tag{2.1}$$

where $V_p\left(\theta_{l,c}\right)$ and $V_\alpha\left(\theta_{l,c}\right)$ are interaction potentials of the electric field with the permanent dipole moment of the molecule and the induced dipole moment of the molecule, respectively. In our case, oscillating electric field has the time period 2.66 fs at 800nm. Oscillation period of the laser field is faster than the rotational period of the molecule (in ps scale), so the interaction potential due to the permanent dipole moment

$V_p\left(\theta_{l,c}\right)$ is averaged zero [59]. Then the only contribution left is interaction potential of the field with the induced dipole moment of the molecule.

From now on, we examine the molecular alignment of linear molecules by linearly and circularly polarized electric field, and let's consider these both of linearly and circularly polarized cases and give the theory behind them.

2.2.1 Nonresonant dipole potential $V_{L,C}(t)$

The nonresonant dipole potential $V_{L,C}(t)$, for each polarization induced by an electric field $E(t)$, is [60,61]

$$V_{L,C}(t) = -\frac{1}{2}\alpha_{L,C}E^2(t) \ , \tag{2.2}$$

where $\alpha_{L,C}$ is effective polarizabilities in case of the linearly and circularly polarized light. The alignment of the molecule is described in spherical coordinates and we determine a laboratory fixed Z axis for each of the linear and circular polarization. Conventionally, we choose Z axis parallel to the electric field vector of linearly polarized light and parallel to the propagation direction of the circularly polarized light.

The polarizability tensor of a linear molecule is given with the expression

$$\alpha = \begin{pmatrix} \alpha_{xx} & 0 & 0 \\ 0 & \alpha_{yy} & 0 \\ 0 & 0 & \alpha_{zz} \end{pmatrix}$$

where α_{xx} is the static polarizability along the molecular axis x due to an electric field applied along x axis in the molecular frame. The induced dipole moment in the lab frame is

$$\mu = \mu_X^{ind}\hat{i} + \mu_Y^{ind}\hat{j} + \mu_Z^{ind}\hat{k} \ . \tag{2.3}$$

Then only taking into consideration the dipole moment in the Z direction, the induced dipole moment can be expressed as

$$\mu_Z^{ind} = \mu_x^{ind}\Lambda_{Zx} + \mu_y^{ind}\Lambda_{Zy} + \mu_z^{ind}\Lambda_{Zz} \ , \tag{2.4}$$

where Λ_{Gg} are the Euler rotation angles for the lab fixed axis G and body fixed axis g. In the molecular frame, the induced dipole moment $\mu_g^{ind} = \alpha_{gg}E_g$ can be written in the equation (2.4) as

$$\mu_Z^{ind} = \alpha_{xx} E_x \Lambda_{Zx} + \alpha_{yy} E_y \Lambda_{Zy} + \alpha_{zz} E_z \Lambda_{Zz} . \quad (2.5)$$

The expression for the electric field along a molecular axis g due to the electric field along a lab fixed axis XYZ becomes

$$E_g = E_X \Lambda_{Xg} + E_Y \Lambda_{Yg} + E_Z \Lambda_{Zg} \ . \quad (2.6)$$

For linearly polarized field, the field is only applied along the Z direction. The expression for the electric field reduces to $E_g = E_Z \Lambda_{Zg}$. Then, the induced dipole moment defined as

$$\mu_Z^{ind} = \alpha_{xx} E_Z \Lambda_{Zx}^2 + \alpha_{yy} E_Z \Lambda_{Zy}^2 + \alpha_{zz} E_Z \Lambda_{Zz}^2 \ . \quad (2.7)$$

For linear molecules, the polarizability components are $\alpha_{xx} = \alpha_{yy} = \alpha_\perp$ and $\alpha_{zz} = \alpha_\parallel$, where $\alpha_\perp$ and $\alpha_\parallel$ are polarizabilities perpendicular and parallel to the molecular axis, respectively. Plugging this into the equation(2.7), the induced dipole moment expresses

$$\mu_Z^{ind} = \left[\alpha_\perp \left(\Lambda_{Zx}^2 + \Lambda_{Zy}^2 \right) + \alpha_\parallel \Lambda_{Zz}^2 \right] E_Z . \quad (2.8)$$

By applying $\sum_g \Lambda_{Zg}^2 = 1$, the expression for the induced dipole moment becomes

$$\mu_Z^{ind} = \left[\Delta\alpha \cos^2 \theta_l + \alpha_\perp \right] E_Z . \tag{2.9}$$

Finally, we obtain

$$\alpha_L = \Delta\alpha \cos^2 \theta_l + \alpha_\perp , \tag{2.10}$$

where $\Delta\alpha = \alpha_{||} - \alpha_\perp$ is anisotropic polarizability of the molecule. Assuming complete alignment case between the molecular axis and the electric field, for a molecule in a linearly polarized laser field where $\theta_l = 0$; the maximum effective polarizability is $\alpha_L = \alpha_{||}$, whereas in the complete anti-alignment case where $\theta_l = 90$, the minimum effective polarizability is $\alpha_L = \alpha_\perp$.

The complete expression for the induced dipole potential of a linear molecule in a linearly polarized field along the Z axis is [62-64]

$$V_L(t) = -\frac{1}{2}\left[\Delta\alpha \cos^2 \theta_l + \alpha_\perp \right] E^2(t) . \tag{2.11}$$

For circularly polarized light, the procedure is similar except the nonzero terms. The induced dipole moment is

$$\mu = \mu_X^{ind} \hat{i} + \mu_Y^{ind} \hat{j} \tag{2.12}$$

with

$$\begin{aligned}\mu_X^{ind} &= \left(\alpha_{xx}\Lambda_{Xx}^2 + \alpha_{yy}\Lambda_{Xy}^2 + \alpha_{zz}\Lambda_{Xz}^2\right)E_X \\ &\\ \mu_Y^{ind} &= \left(\alpha_{xx}\Lambda_{Yx}^2 + \alpha_{yy}\Lambda_{Yy}^2 + \alpha_{zz}\Lambda_{Yz}^2\right)E_Y\end{aligned} \quad . \tag{2.13}$$

The lab frame effective polarizability with $\left|E_X\right| = \left|E_Y\right| = E$ is

$$\frac{\mu_X^{ind} + \mu_Y^{ind}}{E} = \alpha_\perp\left(\Lambda_{Xx}^2 + \Lambda_{Xy}^2 + \Lambda_{Yx}^2 + \Lambda_{Yy}^2\right) + \alpha_\parallel\left(\Lambda_{Xz}^2 + \Lambda_{Yz}^2\right) \tag{2.14}$$

By using $\sum_g \Lambda_{Zg}^2 = 1$ and $\sum_G \Lambda_{Gz}^2 = 1$[65], effective polarizability can be written as

$$\alpha_C = \frac{1}{2}\left[\alpha_\perp\left(1 + \cos^2\theta_c\right) + \alpha_\parallel \sin^2\theta_c\right] \tag{2.15}$$

For the complete alignment for the molecule in a circularly polarized laser field with $\theta_c = 90$; the maximum effective polarizability is $\alpha_c = \frac{\alpha_\parallel + \alpha_\perp}{2}$, whereas for the complete anti-alignment where $\theta_c = 0$, the minimum effective polarizability is $\alpha_c = \alpha_\perp$.

The total expression due to circularly polarized light is [62-64,66]

$$V_C(t) = -\frac{1}{4}\left[\alpha_\parallel + \alpha_\perp - \Delta\alpha\cos^2\theta_c\right]E^2(t). \tag{2.16}$$

2.2.2 Solving TDSE of the system

In order to understand the details of the molecular dynamics of a molecule in an intense laser field, one needs to solve time dependent Schrodinger equation (TDSE) [67]:

$$i\hbar \frac{\partial}{\partial t}\Phi_{JM}(t) = \left(H_0 + V_{L,C}(t)\right)\Phi_{JM}(t) \tag{2.17}$$

where $\mathrm{H}_0 = \mathrm{B}\hat{J}^2$ with the rotational constant B and the squared the angular momentum operator $\hat{J}^2$, is the field-free Hamiltonian of the molecule and $V_{L,C}(t)$ is the potential experienced by the molecule in the presence of an electric field which is called pump pulse and defined here as a subscript *L* and *C* for linearly and circularly polarized field, respectively. Quantum mechanically, in the absence of an electric field, simply a molecule is described as a rigid rotor and the solutions of the rigid rotor equation are spherical harmonics $Y_{JM}(\theta,\varphi)$, where *J* and *M* are the quantum numbers stand for the angular momentum quantum number and its projection onto the Z axis, respectively.

By using eqs. (2.11) and (2.16), Hamiltonian takes form [68]:

$$\begin{aligned} H(t) &= B\hat{J}^2 - \frac{E^2(t)}{2}\left(\alpha_\perp + \Delta\alpha\cos^2\theta\right) \\ &= B\left[\left(\hat{J}^2 - \omega_\perp(t)\right) - \Delta\omega(t)\cos^2\theta\right] \end{aligned} \tag{2.18}$$

for linearly polarized light, and

$$H(t) = B\hat{J}^2 - \frac{E^2(t)}{4}\left(\alpha_{\parallel} + \alpha_{\perp} - \Delta\alpha\cos^2\theta_c\right)$$
$$= B\left[\left(\hat{J}^2 - \omega_{\perp}^c(t) - \omega_{\parallel}^c(t)\right) - \Delta\omega^c(t)\cos^2\theta\right] \tag{2.19}$$

for circularly polarized light with dimensionless interaction parameters,

$\omega_{\parallel}(t) = \alpha_{\parallel}E^2(t)/2B$, $\omega_{\perp}(t) = \alpha_{\perp}E^2(t)/2B$, $\Delta\omega(t) = \omega_{\parallel} - \omega_{\perp}$, $\omega_{\parallel,\perp}^c(t) = \alpha_{\parallel,\perp}E^2(t)/4B$, and $\Delta\omega^c(t) = \omega_{\parallel} - \omega_{\perp} = \Delta\alpha E^2(t)/4B$ [69,70].

The rotational wave function $\Phi(t)$ can be expressed as a superposition of rotational states of the molecule $|JM\rangle$ with eigen energy $E_J = B_i\left[J(J+1)\right]^i$ [71]. By considering an initial state $|\Phi_{J_0M_0}(t)\rangle$, the rotational wave function can be written as superposition of rotational wave packets [67,72],

$$|\Phi_{J_0M_0}(t)\rangle = \sum_{JM} d_{JM}^{J_0M_0}(t)\exp\left(-i\frac{E_J t}{\hbar}\right)|JM\rangle\ , \tag{2.20}$$

where $d_{JM}^{J_0M_0}(t)$ are the expansion coefficients determined by solving differential equations for linearly polarized light [70] as

$$i\frac{\hbar}{B}d'^{J_0M_0}_{JM}(t)=d^{J_0M_0}_{JM}(t)\langle JM|\left(\hat{J}^2-\omega_\perp(t)\right)|JM\rangle$$
$$-\sum_{J'M'}d^{J_0M_0}_{J'M'}(t)\langle JM|\Delta\omega(t)\cos^2\theta_l|J'M'\rangle\exp\left(-\frac{i(E_{J'}-E_J)t}{\hbar}\right) \quad (2.21)$$

and for circularly polarized light,

$$i\frac{\hbar}{B}d'^{J_0M_0}_{JM}(t)=d^{J_0M_0}_{JM}(t)\langle JM|\left(\hat{J}^2-\omega^c_\perp(t)-\omega^c_\parallel(t)\right)|JM\rangle$$
$$-\sum_{J'M'}d^{J_0M_0}_{J'M'}(t)\langle JM|\Delta\omega^c(t)\cos^2\theta_c|J'M'\rangle\exp\left(-\frac{i(E_{J'}-E_J)t}{\hbar}\right) \quad (2.22)$$

The constant term in the Hamiltonian can be dropped for convenience due to not providing any torque. Then taking into account of the only term left which is angular dependent, the solution can be written as the superposition of the rotational states $|JM\rangle$ by the selection rules $\Delta J=0,\pm2$ (with the same parity, even or odd) and $\Delta M=0$ [70]. The expression for the linearly polarized light is given by [70,73,74]

$$i\frac{\hbar}{B}d'^{J_0M_0}_{JM}(t) = -d^{J_0M_0}_{J-2,M_0}(t)\Delta\omega(t)\langle J,M_0|\cos^2\theta_l|J-2,M_0\rangle\exp\left(-i\left(E_{J-2}-E_J\right)t/\hbar\right)$$

$$-d^{J_0M_0}_{J,M_0}(t)\Delta\omega(t)\langle JM_0|\cos^2\theta_l|JM_0\rangle + d^{J_0M_0}_{JM_0}(t)(J(J+1)-\omega_\perp(t))$$

$$-d^{J_0M_0}_{J+2,M_0}(t)\Delta\omega(t)\langle J,M_0|\cos^2\theta_l|J+2,M_0\rangle\exp\left(-i\left(E_{J+2}-E_J\right)t/\hbar\right)$$

(2.23)

and for circularly polarized light

$$i\frac{\hbar}{B}d'^{J_0M_0}_{JM}(t) = -d^{J_0M_0}_{J-2,M_0}(t)\Delta\omega^c(t)\langle J,M_0|\cos^2\theta_c|J-2,M_0\rangle\exp\left(-i\left(E_{J-2}-E_J\right)t/\hbar\right)$$

$$-d^{J_0M_0}_{J,M_0}(t)\Delta\omega^c(t)\langle JM_0|\cos^2\theta_c|JM_0\rangle + d^{J_0M_0}_{JM_0}(t)(J(J+1)-\omega^c_\perp(t)-\omega^c_\parallel(t)) \quad .$$

$$-d^{J_0M_0}_{J+2,M_0}(t)\Delta\omega^c(t)\langle J,M_0|\cos^2\theta_c|J+2,M_0\rangle\exp\left(-i\left(E_{J+2}-E_J\right)t/\hbar\right)$$

(2.24)

The matrix elements are the same for linearly and circularly polarized light [75,76] as

$$\left\langle J,M_0\left|\cos^2\theta\right|J-2,M_0\right\rangle=\frac{1}{2J-1}\sqrt{\frac{\left(\left(J-1\right)^2-M_0^2\right)\left(J^2-M_0^2\right)}{\left(2J-3\right)\left(2J+1\right)}}$$

$$\left\langle JM_0\left|\cos^2\theta\right|JM_0\right\rangle=\frac{1}{3}+\frac{2}{3}\left[\frac{J\left(J+1\right)-3M_0^2}{\left(2J-1\right)\left(2J+3\right)}\right] \quad . \quad (2.25)$$

$$\left\langle J,M_0\left|\cos^2\theta\right|J+2,M_0\right\rangle=\frac{1}{2J+3}\sqrt{\frac{\left(\left(J+1\right)^2-M_0^2\right)\left(\left(J+2\right)^2-M_0^2\right)}{\left(2J+1\right)\left(2J+5\right)}}$$

2.2.3 Degree of molecular alignment

The degree of molecular alignment is characterized by the expectation value of $\cos^2\theta_{l,c}$ $\left(\left\langle\cos^2\theta_{l,c}\right\rangle\right)$[59] . For a linear molecule with the initial state $\left|J_0M_0\right\rangle$ and the eigenvalue $E_J=BJ\left(J+1\right)$, $\left\langle\cos^2\theta_{l,c}\right\rangle$ can be written as

$$\begin{aligned}\left\langle\cos^2\theta_{l,c}\right\rangle_{J_0M_0}\left(t\right)&=\left\langle\Phi_{J_0M_0}\left(t\right)\left|\cos^2\theta_{l,c}\right|\Phi_{J_0M_0}\left(t\right)\right\rangle\\&=\sum_J d^{J_0M_0*}_{J-2,M_0}\left(t\right)d^{J_0M_0}_{J,M_0}\left(t\right)\left\langle J,M_0\left|\cos^2\theta_{l,c}\right|J-2,M_0\right\rangle\exp\left(-iB\left(4J-2\right)t/\hbar\right)\\&+\sum_J\left|d^{J_0M_0}_{JM_0}\left(t\right)\right|^2\left\langle JM_0\left|\cos^2\theta_{l,c}\right|JM_0\right\rangle\\&+\sum_J d^{J_0M_0*}_{J+2,M_0}\left(t\right)d^{J_0M_0}_{JM_0}\left(t\right)\left\langle J,M_0\left|\cos^2\theta_{l,c}\right|J+2,M_0\right\rangle\exp\left(-iB\left(4J+6\right)t/\hbar\right)\end{aligned}$$

. (2.26)

Equation (2.26) can be reorganized in a symmetric form by shifting $J \to J+2$ in the first term,

$$\left\langle \cos^2\theta_{l,c} \right\rangle_{J_0M_0}(t) = \sum_{J=2}^{J_{\max}} d^{J_0M_0*}_{J-2,M_0}(t)\, d^{J_0M_0}_{JM_0}(t) \left\langle J, M_0 \left| \cos^2\theta_{l,c} \right| J-2, M_0 \right\rangle \exp\left(-iB\left(4J+6\right)t/\hbar\right)$$

$$+\sum_{J} \left| d^{J_0M_0}_{JM_0}(t) \right|^2 \left\langle JM_0 \left| \cos^2\theta_{l,c} \right| JM_0 \right\rangle$$

$$+\sum_{J=0}^{J_{\max}} d^{J_0M_0*}_{J+2,M_0}(t)\, d^{J_0M_0}_{JM_0}(t) \left\langle J, M_0 \left| \cos^2\theta_{l,c} \right| J+2, M_0 \right\rangle \exp\left(-iB\left(4J+6\right)t/\hbar\right)$$

(2.27)

where $J_{\max}$ stand for the maximum number of excited states.

2.2.3.1 Rotational temperature

The rotational temperature of the molecules is critical in determining the amount of alignment observed. When we consider an ensemble of molecules before the interaction with the linearly polarized laser pulse, assuming the gas ensemble is in thermal equilibrium initially we can define the expectation value of the alignment degree by Boltzmann distribution. Boltzmann distribution of the ensemble whose initial rotational states $\left| J_0M_0 \right\rangle$ with $J_0 = 0,1,2,...$ and $M = -J_0 - \left(J_0 - 1\right), ..., 0, \left(J_0 - 1\right), J_0$ is

$$P_{J_0} \sim (2J_0+1)\exp\left(-\frac{E_{J_0}}{kT}\right) \tag{2.28}$$

where E_{J_0} accounts for the rotational energy of the state $|J_0 M_0\rangle$. In the Boltzmann distribution, the term $(2J_0+1)$ comes from the degeneracy for each initial rotational state J_0.

If we consider a molecule with two identical nuclei, the additional factor g_{J_0} originating from the nuclear spin statistics appears in the Boltzmann distribution [77,78] and this factor determines relative weight between even and odd rotational states. Equation (2.28) is written with this additional factor as

$$P_{J_0} \sim g_{J_0}(2J_0+1)\exp\left(-\frac{E_{J_0}}{kT}\right). \tag{2.29}$$

Finally, the degree of alignment of an ensemble at a rotational temperature T in thermal equilibrium can be written by averaging the degree of alignment of a single rotational state Eq. (2.27) over the Boltzmann distribution

$$\left\langle\left\langle \cos^2\theta_{l,c}\right\rangle\right\rangle(t) = \frac{\sum_{J_0}^{J_{\max}}\sum_{M_0=-J_0}^{J_0} g_{J_0}\left\langle\cos^2\theta_{l,c}\right\rangle_{J_0M_0}(t)\exp\left(-BJ_0(J_0+1)/kT\right)}{\sum_{J_0}^{J_{\max}}\sum_{M_0=-J_0}^{J_0} g_{J_0}\exp\left(-BJ_0(J_0+1)/kT\right)} \tag{2.30}$$

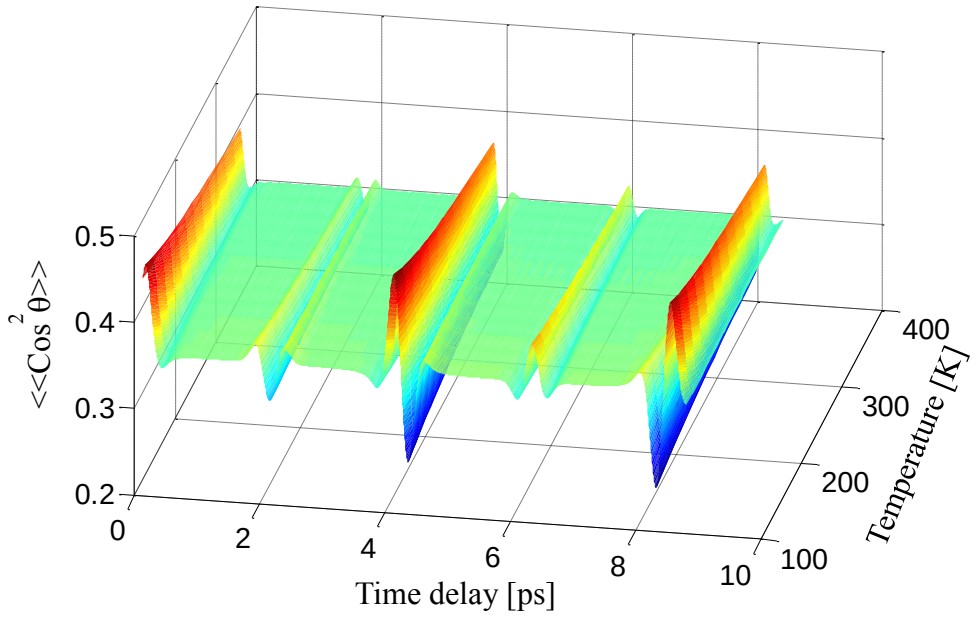

Figure 2.2 Calculated molecular dynamic of N_2 as a function of initial temperatures. The peak intensity of laser field is $2x10^{13}W/cm^2$.

where $\left\langle \cos^2 \theta_{l,c} \right\rangle_{J_0 M_0}(t)$ is the degree of alignment of a single initial state.

The degree of alignment increases when the temperature decreases and vice versa as seen in Figure 2.2. The *J* population is dependent on the laser intensity as seen in a previous calculation [79], so we calculated time dependence of the alignment factor of N_2 at room temperature for different intensities as seen in Figure 2.3. For the peak intensity of $2x10^{13}W/cm^2$, which we used in our alignment experiments for nitrogen molecule, time dependence of the alignment factor of N_2 at room temperature are shown in Figure 2.4 for maximum excited rotational states J_{max}.

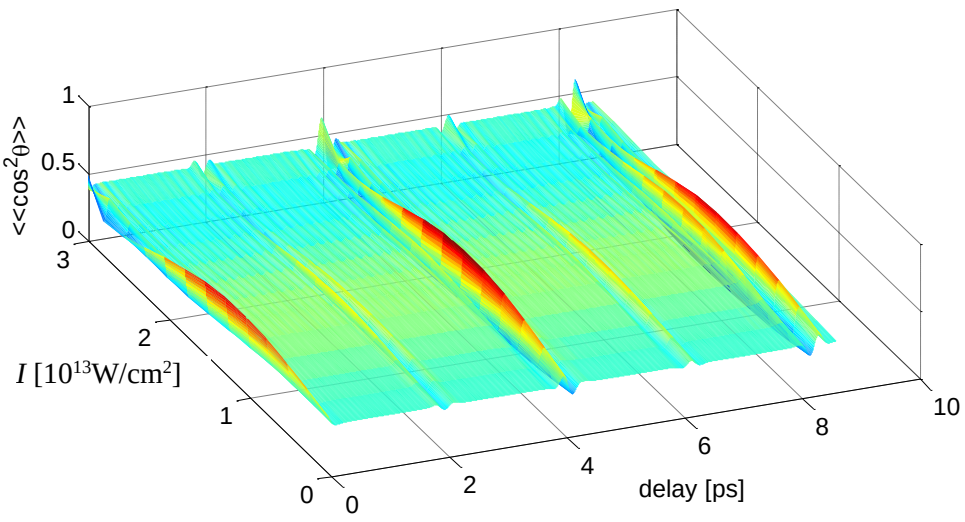

Figure 2.3 Time dependence of the alignment factor of N_2 at room temperature for different intensities at initial room temperature

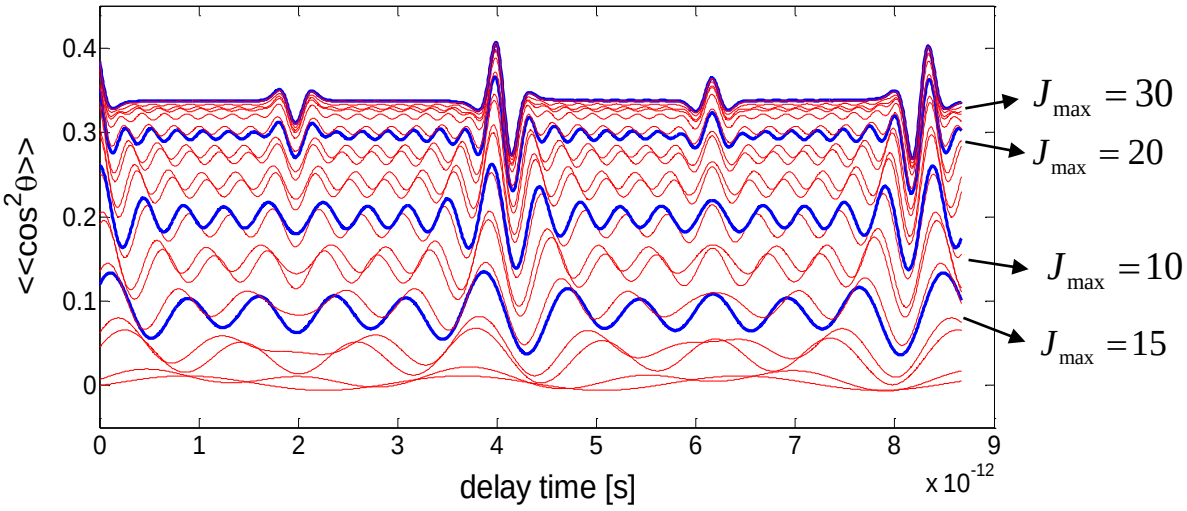

Figure 2.4 Calculated results for time dependence of the alignment factor of N_2 molecules at room temperature for different maximum excited rotational states J_{max}. The peak intensity of laser field is $2x10^{13}W/cm^2$ with 50fs, and the initial temperature is 300K.

2.2.3.2 Nuclear spin effect

For complete description, the influence of nuclear spin of atoms constituting the molecule must be taken into account. In heteronuclear diatomic molecules interchange of nuclei under symmetry operation did not apply because molecule is asymmetrical.

A total wave function of a molecule Ψ_{tot} can be factorized as $\Psi_{tot} = \psi_{el} \times \psi_{vib} \times \psi_{rot} \times \psi_{ns}$, where ψ_{el} electronic wave function, ψ_{vib} vibrational wave function, ψ_{rot} rotational wave function, and ψ_{ns} nuclear spin wave function of the molecule. A homonuclear diatomic molecule has a center of symmetry and the total wave function Ψ_{tot} should be symmetric with respect to exchange of nuclei if nuclear spin, *I* is

integral or zero (bosonic), and antisymmetric with respect to exchange of nuclei if nuclear spin, I is half-integral (fermionic). In the Eq. (2.30) the additional factor g_{J_0} appearing in the Boltzmann distribution that comes from the nuclear spin statistics as follow:

For gerade electronic states, bosonic nuclei have:

$$\begin{aligned} g_{J_0} &= (2I+1)(I+1) \text{ if } J \text{ is even} \\ &= (2I+1)(I) \text{ if } J \text{ is odd} \end{aligned} \tag{2.31}$$

and fermionic nuclei have:

$$\begin{aligned} g_{J_0} &= (2I+1)I \text{ if } J \text{ is even} \\ &= (2I+1)(I+1) \text{ if } J \text{ is odd} \end{aligned} \tag{2.32}$$

The ratio of odd to even states is reversed for ungerade electronic states. Here, I is the nuclear spin of indistinguishable nuclei exchanged during rotation [78]. Figure 2.5 shows an example of time dependence of the alignment factor of N_2 molecules at room temperature for odd rotational states only, even rotational states only, and 1:2 mixture of odd:even rotational states.

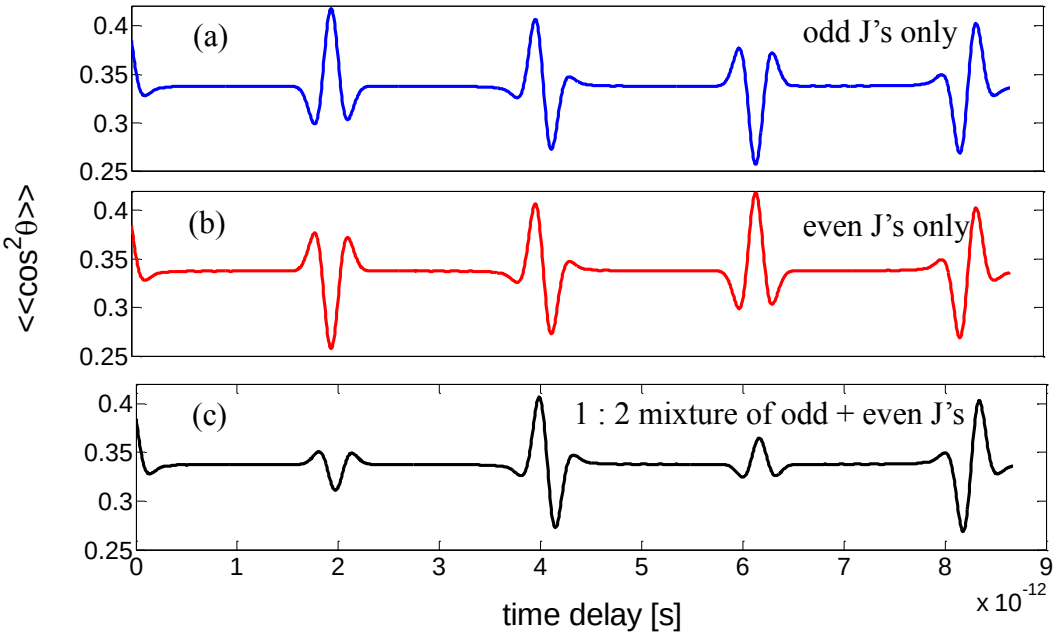

Figure 2.5 Calculation results for time dependence of the alignment factor of N_2 molecules at room temperature for: (a) odd rotational states only, (b) even rotational states only, and (c) 1:2 mixture of odd:even rotational states. The laser parameters and the initial temperature are similar with Fig. 2.4.

2.2.4 Revival structures

Recall the time dependence of the observable of molecular alignment $\left\langle\left\langle \cos^2\theta_{l,c}\right\rangle\right\rangle$ based on the rotational wave packet evolution in time (Eq. (2.20)). The energy of linear molecules are given with the expression $E_J = hBcJ(J+1)$. The rotational energies are quantized, so the rotational wave packet periodically reproduces itself when the oscillating

terms collect a phase over a period of time at the integer multiples of 2π, which is at the integer multiples of $T_{rev} = 1/(2Bc)$ and called "rotational revival time". Thus, the wave function is periodic $\Phi(t) = \Phi(t + T_{rev})$ and corresponding observable of the molecular alignment $\langle\langle \cos^2 \theta_{l,c} \rangle\rangle$ considered in our interest here is also periodic. Figure 2.6 shows nonadiabatic alignment for five linear molecules with different nuclear statistics. One can also see that for the terms with $J \to J \pm 2$, the time dependent phase factor associated with $\langle\langle \cos^2 \theta_{l,c} \rangle\rangle$ as

$$\phi_{J,J\pm2} = \exp\left(-i\pi n(4J+6)\right) \tag{2.33}$$

where the time n is given in units of $T_{rev} = 1/(2Bc)$. At integer revivals, $n =$ 0, 1, 2, …, the phase term $\phi_{J,J\pm2} = 1$ for all the *J* quantum numbers. At half revival $n = 1/2$ the phase terms are π shifted for all of the *J*'s, resulting in the phase term $\phi_{J,J\pm2} = -1$, and thus overall distribution has the same magnitude but peaking in the negative direction. At quarter revivals, since the phase term $\phi_{J,J\pm2}$ depends on the even or odd parity of *J* state, the situation requires more analysis. At $n = 1/4$ while the phase term $\phi_{J,J\pm2} = i$ for even *J* states, $\phi_{J,J\pm2} = -i$ for odd *J* states. The even and odd states contribute to the signal, however their phases are shifted by π, and therefore they interfere destructively. Moreover, the time-dependent signal at integer revivals is phase-shifted by $\pi/2$ with

regarding to the signal observed at half revivals. At three-quarters revivals the phases are shifted by $\pi/2$ with regarding to the quarter revival. Their peak amplitudes depend on nuclear spin statistics as we described in section 2.2.3.2. The time-dependent alignment signal due to even and odd parity at the quarter and the three-quarter revival times will be also discussed in the analysis of our experimental data in terms of nuclear spin statistics. It is important to note that the alignment degree is sensitive to molecular properties (i.e. rotational constant B and nuclear statistics g_{J_0}), pulse parameters (peak intensity I and pulse duration τ), and initial ensemble temperature (T).

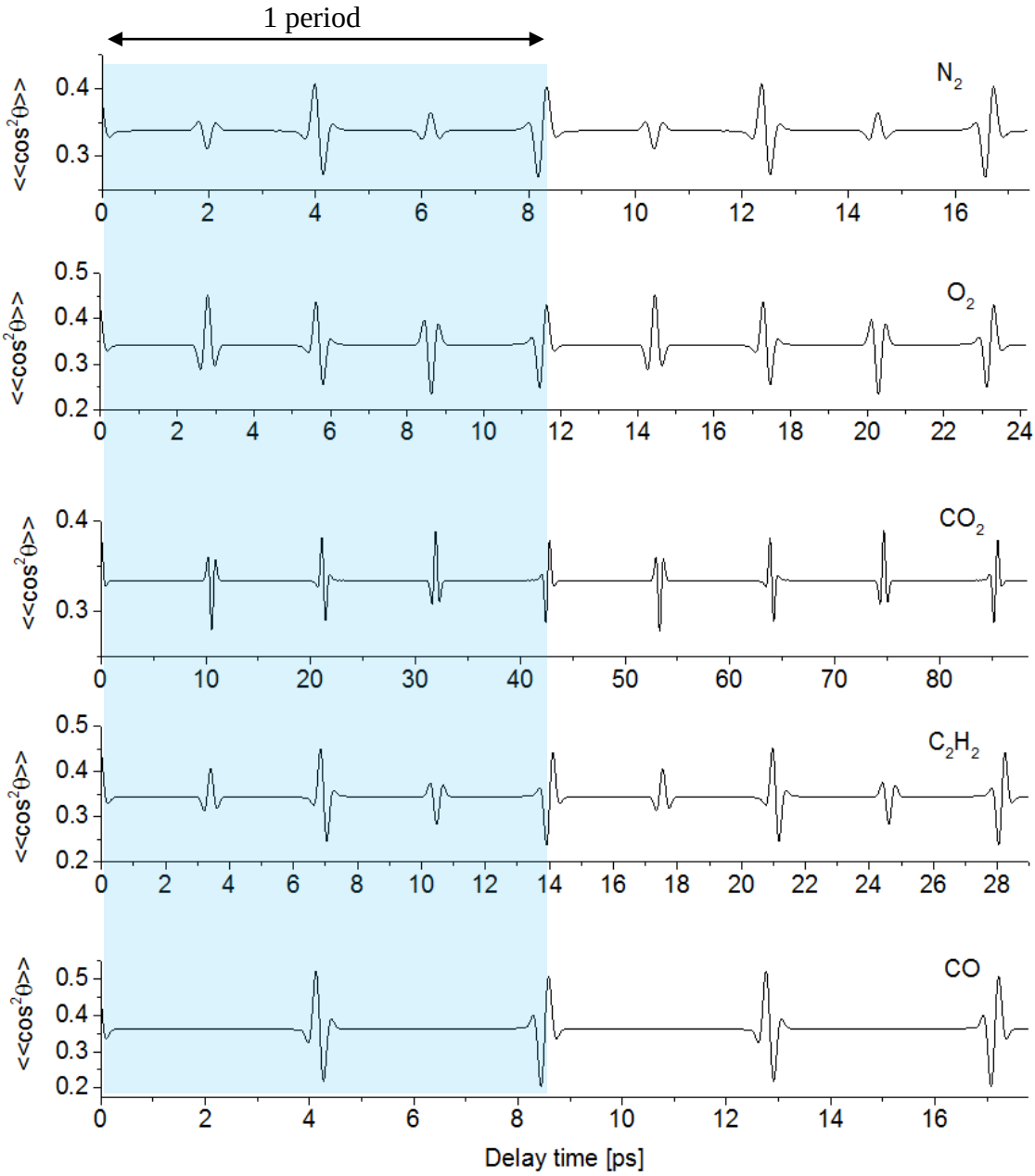

Figure 2.6 Dynamics of the alignment of N_2, O_2, CO_2, C_2H_2 and CO molecules with an initial temperature 300 K. We use a linearly polarized laser pulse with peak intensity of 2×10^{13} W/cm^2 for N_2, O_2, and CO, 0.9×10^{13} W/cm^2 for CO_2, and 1×10^{13} W/cm^2 for C_2H_2 with FWHM 50 fs.

CHAPTER III

GENERAL DESCRIPTION OF RESEARCH INSTRUMENTATION

The main focus of this chapter is on the laser system and the pulse measurement techniques used in measurements.

3.1 Laser systems

Our laser system includes four interrelated lasers. We labelled them by the manufacturer as Millenia V, Kapteyn-Murnane (KM oscillator), Evolution laser and Spitfire (regenerative amplifier).

3.1.1 Millenia V

The Millennia V is a solid-state, high power, continuous wave (CW) laser that supplies more than 5 W of green 532 nm output, which is obtained by intracavity doubling the frequency of a diode pumped Nd:YAG laser. The frequency doubling is done by a temperature tuned lithium triborate (LBO) crystal. In our system, Millennia V is used to pump the femtosecond Kapteyn-Murnane (KM) oscillator at a continuous optical power of ~4.4 W at 532 nm wavelength.

3.1.2 Kapteyn-Murnane (KM) oscillator

KM is a mode-locked Ti:Sapphire femtosecond oscillator pumped by Millennia V. To achieve the Kerr lens effect, concave mirrors are used which form the telescope with the crystal in the focal plane. In Figure 3.1, Ti:Sapphire femtosecond oscillator is shown, where M1, M2, M3, M4, M5 are the cavity mirrors, and M3 is also the output mirror. The

group velocity dispersion experienced by the laser pulse traveling inside the crystal is compensated by a pair of prisms P1 and P2. The output of the oscillator is a train of pulses emitted in the spectral range from 780 nm to 830 nm; the pulse duration is about 35 fs, the repetition rate is close to 80 MHz, the energy ~5 nJ/pulse and the average power is about 400 mW.

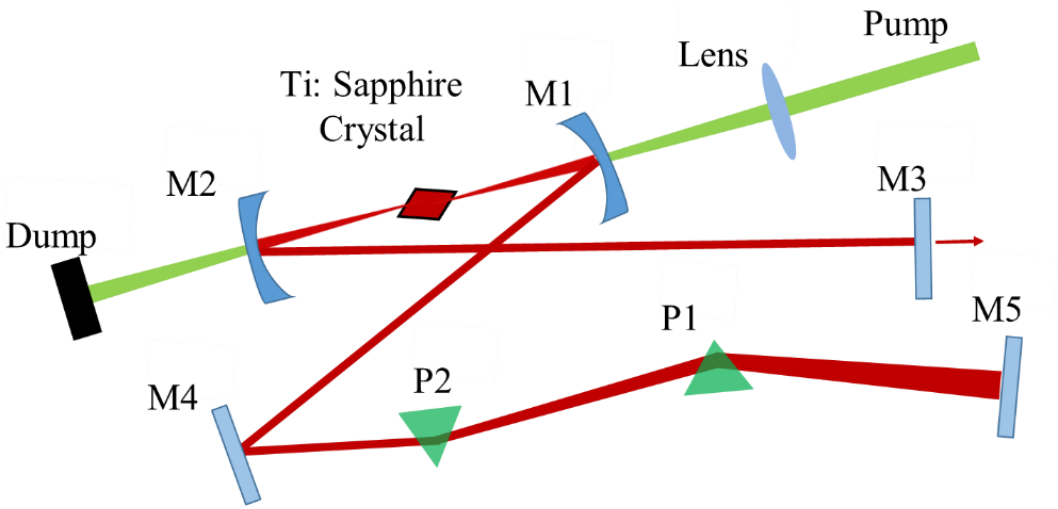

Figure 3.1 The outline of the Ti:sapphire femtosecond oscillator (KM oscillator). M1, M2, M3, M4, M5 are the cavity mirrors, where M3 is at the same time the output coupler. The group velocity dispersion experienced by the laser pulse traveling inside the crystal is compensated by a pair of prisms P1 and P2.

3.1.3 Evolution 15

Evolution is a Q-switched Nd:YAG laser (Spectra Physics, Merlin) at a repetition rate 1 kHz, output power 10 W at 532 nm wavelength with ~10 ns pulse duration. The gain

medium and pump lasers are enclosed inside the laser head and co-located in a directly water cooled resonant cavity. The Evolution is used to pump the spitfire.

3.1.4 Spitfire (regenerative amplifier)

The regenerative amplifier technique is used to amplify femtosecond pulses. In our system (Figure 3.2) [80] it is used to amplify seed pulses (KM Oscillator) that follow with a repetition rate around 80 MHz. The amplifier is pumped by the Evolution laser that has a repetition rate of 1 kHz. Thus, only a small part of the pulses from the oscillator is amplified. The seed pulse is inside the laser cavity when the pump pulse passes through the crystal. When the gain is saturated, the amplified pulses are let out of the cavity. For this reason a fast optical switch that has a response time in the nanosecond range is required.

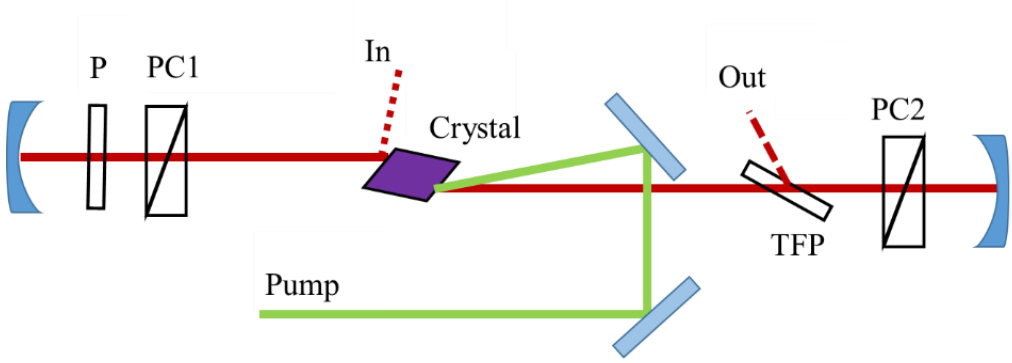

Figure 3.2 Schematic of regenerative cavity

Our Spitfire contains three main parts: stretcher, regenerative cavity and compressor. First, the seed pulses are expanded in the stretcher. A photodiode that is placed behind one of the cavity mirrors helps to monitor the trace of the femtosecond pulses on the oscilloscope. The Pockels cell changes the refractive index of the material under the applied electric field and consequently the polarization, so that an amplified linearly polarized pulse is let out of the cavity. The output of the amplifier is a train of the pulses having average power ~900 mW, repetition rate 1 kHz, pulse energy 0.9 mJ and pulse duration 50 fs. Figure 3.3 depicts the layout of the laser system.

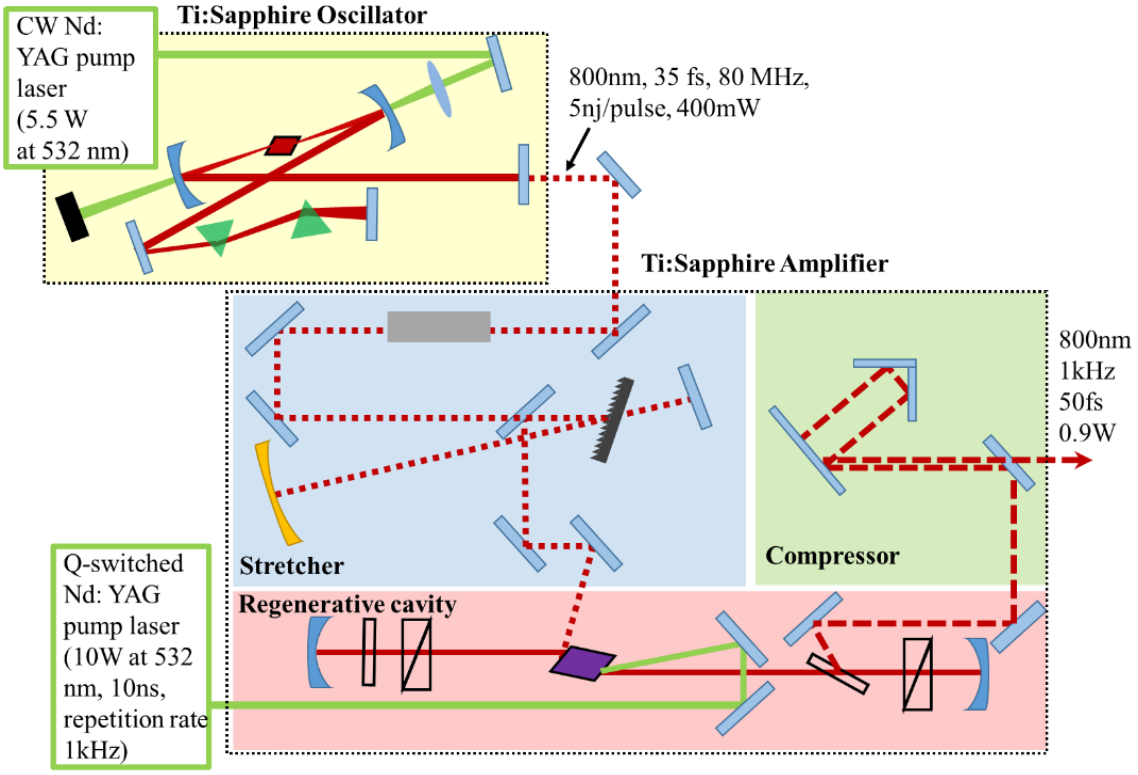

Figure 3.3 The outline of the laser system: Ti:sapphire femtosecond oscillator (KM oscillator) is pumped by a CW optical power of 4.5 W at 532 nm wavelength from Millenia V. Seed femtosecond pulses (800 nm, 35 fs, 80 MHz, 400 mW) are amplified by Ti:Sapphire regenerative amplifier (including stretcher, regenerative cavity, and the compressor), which is pumped by a Q-switched Nd:YAG laser (10 W at 532 nm, 10 ns, 1 kHz).

3.2 Pulse measurement

3.2.1 Frequency Resolved Optical Gating (FROG) – GRENOUILLE

Frequency resolved optical gating (FROG) helps researchers characterize the pulses in the temporal domain. FROG has the ability to measure femtosecond pulse's spectral intensity vs. time. The FROG setup is shown in Figure 3.4; it consists of an auto-correlation unit and a spectrometer. For autocorrelation the laser pulse is split into two replicas, with one delayed with respect to the other; then both are focused and recombined on a nonlinear Second Harmonic Generation (SHG) crystal. The SHG crystal produces twice the frequency of the input laser, and the spectrometer determines the shape and the phase of

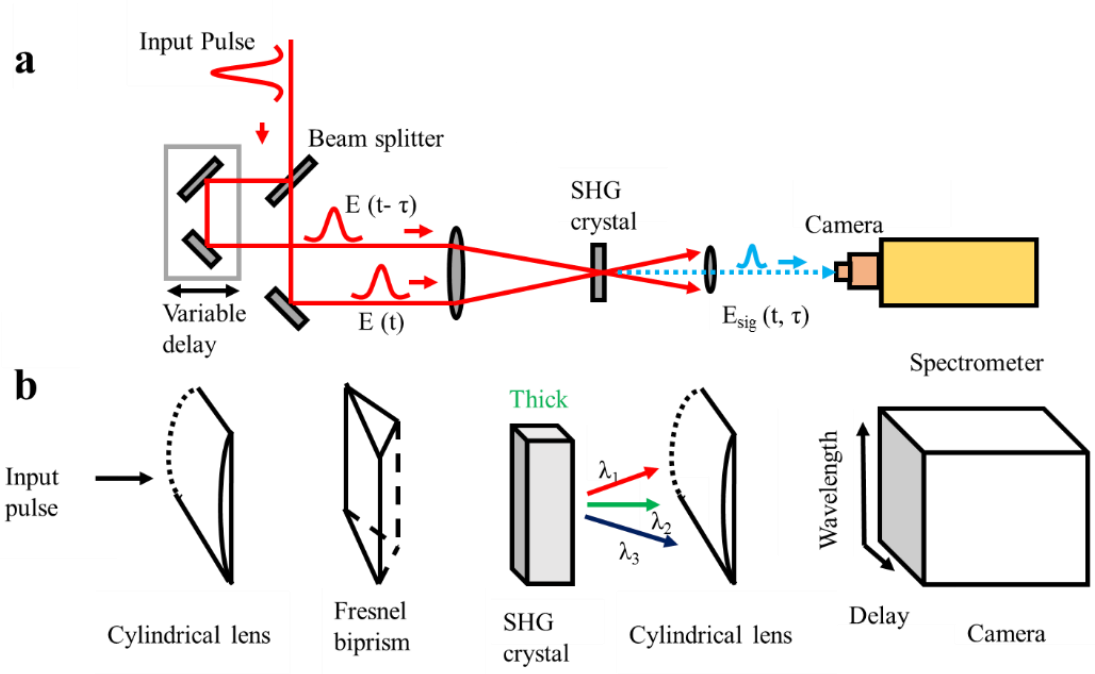

Figure 3.4 (a) Optical scheme of the SHG FROG. (b) GRENOUILLE is the simplest version of the FROG.

the laser pulse. The described FROG update is called GRENOUILLE by Trebino et al. [81,82]. In this device the beam splitter, delay line and beam combining optics is replaced with a Fresnel biprism and a thick SHG crystal. Thus, GRENOUILLE is a combination of two cylindrical lenses, Fresnel biprism, and a SHG crystal. The first lens focuses the beam into the SHG crystal, the Fresnel biprism splits the beam, and delays one pulse relative to the other, and the second lens focuses the beam onto a CCD camera. In Figure 3.5 we show the results of the measurements with the Grenouille (8-20, Swamp Optics).

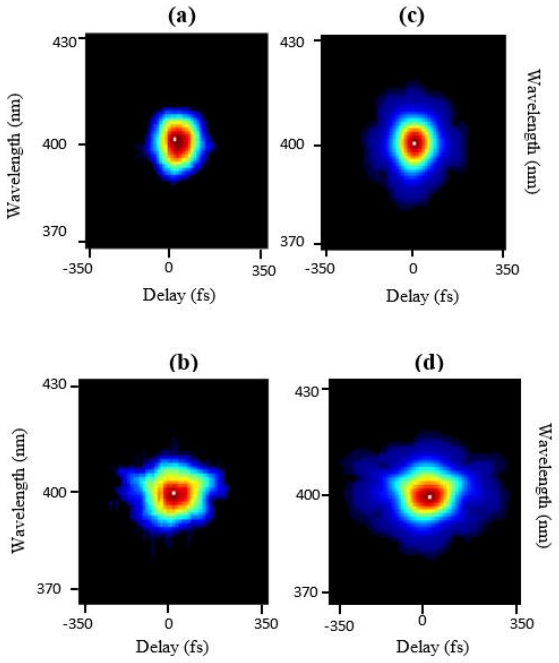

Figure 3.5 (a) Images of femtosecond pulse taken from GRENOUILLE. (a) Compressed pulse at 52 fs. (b) Stretched at 81 fs. (c, d) Retrieved images are from compressed pulse and the stretched pulse, respectively.

CHAPTER IV

NONADIABATIC MOLECULAR ALIGNMENT VIA PHOTOELECTRON IONIZATION YIELDS

This section describes an experiment based on study of the rotational wave packet evolution of linear molecules (N_2, O_2, CO_2, CO, and C_2H_2) aligned by linearly and circularly polarized femtosecond laser pump pulses with detection of electron photoionization yields produced by a variably delayed probe pulse. Initially, we start with background information of ionization processes. Then, we describe our experimental set-up used in the work to create field-free molecular alignment by linearly and circularly polarized femtosecond laser pump pulses and to measure rotational wave packets by the electron photoionization yields produced by a delayed femtosecond probe beam. The detailed experimental results are compared with quantum mechanical calculations and also molecular rotational constants induced with a linearly polarized pump pulse are obtained by fitting experimental data to the calculated results.

4.1 Introduction

Femtosecond laser technology allows aligning molecules and observing the molecular dynamics by using pump-probe technique [8]. Aligning creates a dynamically anisotropic medium evolving in time and changing the interaction with it of laser radiation, which was observed commonly through ionization, fragmentation, and high harmonic generation. In this paper, based on the detection of photoelectron yields in the interaction with the probe

pulse to monitor the alignment process, we measured the impulsively induced rotational wave packet evolution of linear molecules namely N_2, O_2, CO_2, CO, and C_2H_2 by measuring yields of photoionized electrons produced by a variably delayed probe pulse. The alignment process was simulated based on the theoretical approach of Ref [70]. By fitting the model to the experimental data we determined the values of the molecular rotational constants, which are in good agreement with the known literature values.

4.2 Atomic ionization processes

An atom subjected to an intense laser field which has intensity $I > 10^{13}$ W/cm^2, different types of ionization mechanisms are observed depending on the laser intensity, ionization potential of an atom. These ionization processes are called Multiphoton ionization (MPI), Above Threshold Ionization (ATI), Tunnel Ionization (TI), and Over the Barrier Ionization (OTBI) [83]. Laser technology allows the absorption rate of a new photon is much faster than the decay rate, so ionization comes up as a possible situation for an electron by absorbing n photons through transitions from virtual states to exceed ionization potential $\left(n\hbar\omega > I_p\right)$ and reach to the continuum. This process is called as Multiphoton Ionization (MPI) (see Figure 4.1(a)) and observed at the intensities $I > 10^{13}$ W/cm^2. Probability of absorbing n photons (ionization probability) is proportional to the laser intensity $P \approx I^n$ according to the perturbation theory below the intensities 10^{14} W/cm^2.

At the intensities $I \approx 10^{14}$ W/cm^2 a bound electron can be ionized by absorbing more photons than the minimum number n required for ionization. In this process, the resulted photoelectron spectrum shows a series of peaks each separated from the other by

one photon energy indicating that the released electron has more energy than the normal ionization case which require minimum number n photon for ionization of an electron. This significantly nonlinear process is called above-threshold ionization (ATI) and is represented in Figure 4.1(b). Ionization probability for above threshold ionization is proportional to the laser intensity $P \approx I^{n+s}$, where n is the minimum number of photon absorbed and s is additional number of photon absorbed.

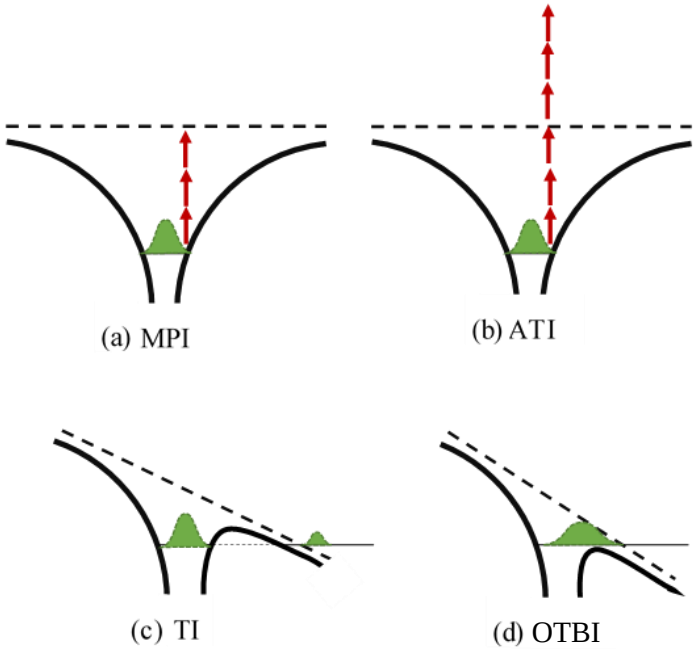

Figure 4.1 Atomic ionization processes: (a) Multiphoton Ionization, (b) Above Threshold Ionization, (c) Tunnel Ionization, (d) Over the Barrier Ionization

At the higher intensities more than $I > 10^{14}$ W/cm^2, the perturbation theory is not valid anymore due to the distortion of the Coulomb potential by the electric field potential of the laser. In this situation, while one side of the Coulomb barrier is raised by strong field the other side of the barrier is lowered. If the tunneling time is less than the half of a period of the field, the electron can tunnel out through the Coulomb potential barrier and escape from an atom or a molecule before the electric field of the laser reverses its direction. This scenario is known as Tunnel Ionization (TI) (see Figure 4.1(c)). At this point, to distinguish the process between Multiphoton Ionization and Tunnel Ionization one introduce as a well-known quantity the Keldyish parameter (γ) which is defined as [84]:

$$\gamma = \sqrt{\frac{I_p}{2U_p}} \tag{4.1}$$

where I_p is the ionization potential of an atom and U_p is the ponderomotive potential which is known as the cycle-averaged quiver energy (or time averaged kinetic energy) of a free electron subjected to an electromagnetic field. The ponderomotive energy is given with the expression [83] below

$$U_p = \frac{E_0^2 e^2}{4 m_e \omega^2} = 9.33 \times 10^{-14} I_0 \left[\mathrm{W/cm^2}\right] \lambda^2 \left[\mu\mathrm{m^2}\right] , \tag{4.2}$$

where E_0 is the amplitude of the electric field, ω is the angular frequency of the laser, e is the charge of the electron and m_e is the mass of the electron. If $\gamma \gg 1$ Multiphoton Ionization, $\gamma \ll 1$ Tunnel ionization becomes dominant process.

When the laser intensity reaches to the higher values $I > 10^{15}$ W/cm^2, the Coulomb potential barrier is lowered by the laser field so that electron is no longer bound and reaches to the continuum. This ionization process is called Over the Barrier ionization (OTBI) and is schematized in Figure 4.1(d).

Similar to an atom, a molecule placed in an intense laser field can be ionized through these ionization processes. In the molecular case, ionization strongly depends on the molecular properties such as molecular symmetry and orientation of the molecular axis with respect to the laser polarization. The molecules investigated were N_2, O_2, CO_2, CO, and C_2H_2 and the properties of the molecules are summarized in Table 1.

Table 1 Relevant parameters for the molecules investigated in the experiment

Molecule	T_{rev}(ps)	I_p(eV)	HOMO symmetry
N_2	8.4	15.6	σ_g
O_2	11.6	12.7	π_g
CO_2	42.7	13.8	π_g
CO	8.64	14.01	σ
C_2H_2	14.2	12.9	π_u

4.3 Experimental procedure

For the measurement of the temporal dependence of the alignment effect, the total photoelectron yield of a gas as a function of the probe pulse delay relative to the linearly polarized and/or circularly polarized pump pulse was measured. We observed the revival structures of the linear molecules N_2, O_2, CO_2, CO, and C_2H_2 in the field-free condition by using a series of pump-probe experiment. The pump-probe setup based on the above threshold ionization (ATI) apparatus is depicted in Figure 4.3 (see also an image of ATI apparatus in Figure 4.2). The apparatus consists of a shaped vacuum chamber with a Pfeiffer Vacuum (TMU 521) turbo molecular pump and Leybold Vacuum IONIVAC (ITR 200 S) ion gauge to maintain and monitor the vacuum pressure, respectively. The vacuum chamber was filled with one of the gases (N_2, O_2, CO_2, CO, or C_2H_2 from Matheson TRIGAS, with purities of 99.9995%, 99.997%, 99.99%, 99.9%, 99.6%, respectively) through a fine adjustable leak valve which allows the introduction of the gas at desired pressure for a given vacuum pumping rate. The pressure of the vacuum chamber was adjusted to 6×10^{-6} mbar and was about three orders of magnitude higher than the background pressure in the ionization chamber.

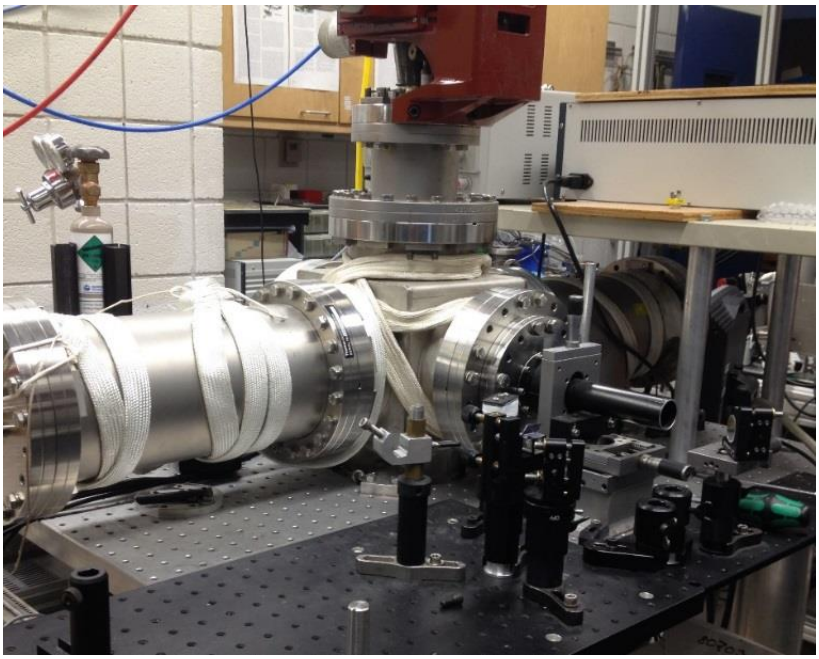

Figure 4.2. Experimental apparatus.

The initial horizontally polarized light (with pulse duration of ~50fs, central wavelength of 800 nm, and output energy of ~1 mJ per pulse at a 1 kHz repetition rate) was split by a beam-splitter into two beams as pump and probe pulses with about equal intensities. Since we did sets of experiment with linearly and circularly polarized pump pulses, we placed a half-wave plate into the pump arm for assuring the proper linear polarization and quarter wave plate for circular polarization of the pump pulse (Figure 4.4). We also used a polarizer for adjusting the intensity of pump beams. Experimentally, the nature of the signal of aligned molecules depends on the time delay between linearly/circularly polarized pump and linearly polarized probe laser pulses, so the time

delay between the pump and probe pulses was precisely adjusted by using an optical variable time delay with a translational stage controlled by a stepping motor (Newport, Model 301), which provided the high resolution of ~1/3 fs. Another beam-splitter was used to recombine the two beams. The laser beams were focused by a 20cm achromatic lens into the vacuum chamber through CVI Melles Griot (W2-PW1-2012-UV-670-1064-0) window. While the pump pulse created rotational wave packets, the probe pulse with an adjustable time delay with respect to the pump pulse ionized the electrons of molecules in the focus. The temporal compression of the laser pulses in the focus was achieved by maximizing the integrated photoelectron yield while adjusting the grating compressor in the laser amplifier. In the experiment, we kept the probe beam horizontally polarized with the field along the axis connecting the centers of the Del Mar Photonics (MCP-MA34/2) microchannel plate detectors. The ionized electrons ejected along the polarization of the probe laser field were detected by the MCP detectors. The electrons traveled within a μ-metal TOF tube in a field-free region. The photoionized electrons from the entire focal volume with small slits were measured at the detector. The signals from the MCP detectors were amplified by ZKL-2 Mini-Circuits preamplifier. A FAST ComTech MCS6 multiple-event time digitizer with 100 ps time resolution was used for data acquisition by using two channels namely start and stop. Start signal was obtained by a photodiode (PD) placed at the behind one of the mirrors on the pump beam and used for triggering FAST ComTec MCS6 multiscaler (MS) PCI counting card. Stop signal was received through ZKL-2 Mini-Circuits preamplifier which amplified signals come from the MCP detectors.

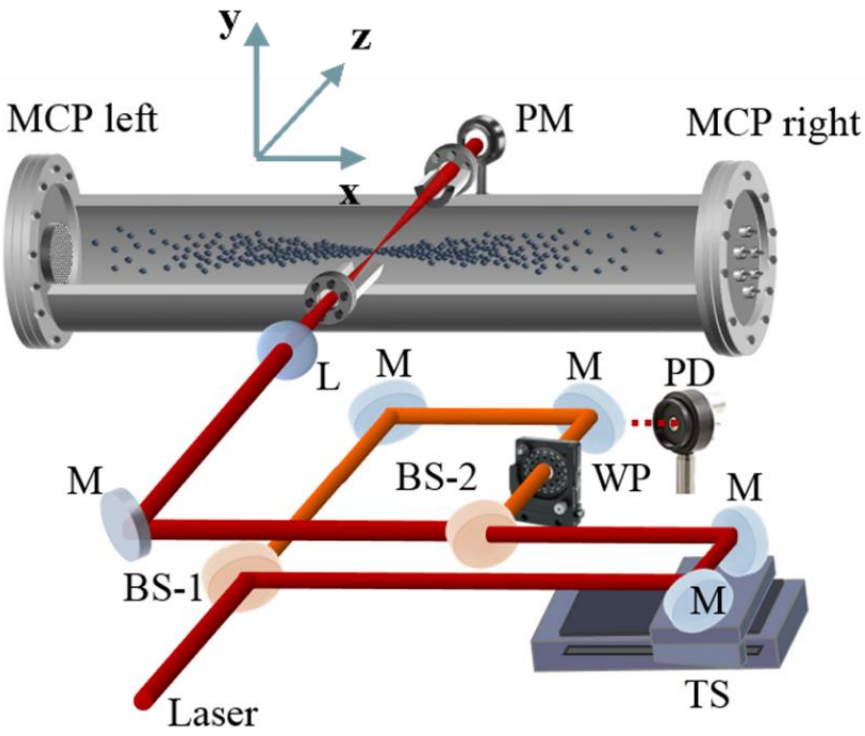

Figure 4.3. Experimental setup. BS: beam-splitters, TS: translational stage, WP: wave plates ($\lambda/2$ wave plate for linearly polarized pump beam and $\lambda/4$ wave plate for circularly polarized pump beam as seen in the inset of Fig. 4.4 (a) and (b)), M: flat mirrors, L: achromatic focusing lens, PM: power meter, MCP: microchannel plates.

The total number of counts depending on the pump-probe delay formed the output signal that was measured. A power meter, Ophir Nova II, was placed at the exit window of the ATI chamber to monitor the laser power during the experiment.

The steps of the experiment were automated by using National Instruments data acquisition card ((NI) DAQ PCI-MIO-16E-4) and Labview 8.5 program for controlling experiment and recording data. The devices automated by Labview program were Newport ESP301 (TS), New Focus Pico driver and rotator, OPHIR NOVA II (PM), FAST ComTec MCS6 multiscaler (MS).

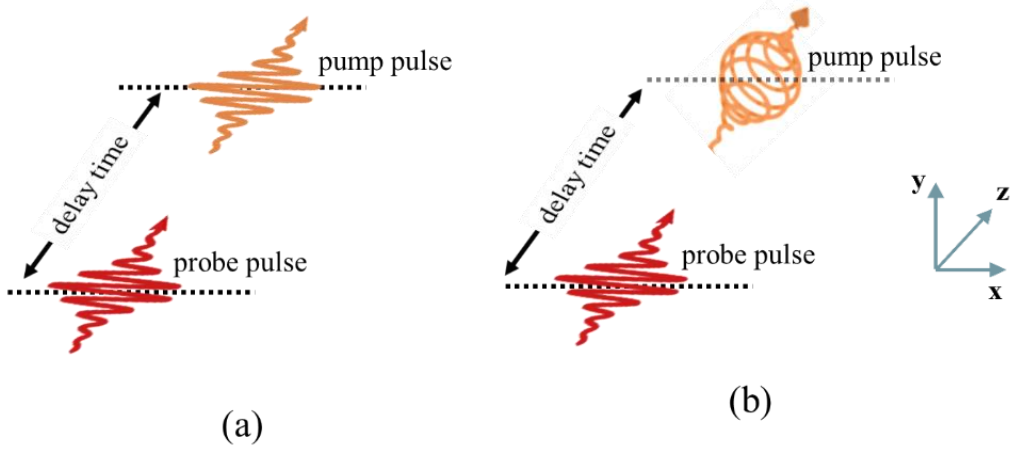

Figure 4.4 Linearly (a) and circularly (b) alignment.

4.4 Results and discussion

In this section we will present experimental results for N_2, O_2, CO_2, CO, and C_2H_2 gases and observed revivals for each gas, followed by interpretation of the observed signals for linearly and circularly polarized pulses. For this interpretation we will consider the total wave function of the linear molecule, which according to the Born-Oppenheimer approximation can be factorized $\Psi_{tot} = \psi_{el} \times \psi_{vib} \times \psi_{rot} \times \psi_{ns}$, as a product of the electronic wave function ψ_{el}, the vibrational wave function ψ_{vib}, the rotational wave function ψ_{rot},

and the nuclear spin wave function ψ_{ns}. We present our experimental results with comparison of the calculated $\left\langle\left\langle \cos^2\theta_{l,c}\right\rangle\right\rangle(t)$ alignment parameter as we calculated in Chapter II depending on our laser parameters and molecular properties.

4.4.1 Molecular alignment by linearly polarized pump pulses

As shown in Figure 4.5, the measured wave packet revival structures and the calculated alignment degree are presented for N_2 molecules aligned by linearly polarized pump pulse. According to the nuclear spin statistics of $^{14}N_2$, the total wave function Ψ_{tot} is symmetric. The linear molecule is in linearly polarized nonresonant electric field oscillating with an optical frequency, so the electronic wave function of ^{14}N, ψ_{el} $(^3\sum_g^+)$, and the vibrational wave function, ψ_{vib} correspond to the ground state, and both are symmetric [12,85]. Therefore, to understand ψ_{rot} behavior, we should consider symmetric and antisymmetric forms of nuclear spin wave function ψ_{ns} of $^{14}N_2$. For Ψ_{tot} to be symmetric both ψ_{rot} and ψ_{ns} must be symmetric or antisymmetric. The nuclear spin of ^{14}N is I=1 and the total nuclear spin of the molecule can take only values I_{tot}=0, 1, or 2, and consequently N_2 has even (I_{tot}=0, 2) and odd (I_{tot} =1) values. For a state with total nuclear spin I_{tot} the degeneracy is 2 I_{tot} +1 and then the statistical weights of even-N_2 and odd-N_2 are 6 and 3, respectively. Thus, the relative ratio of even-N_2 versus odd-N_2 is 2:1 [36]. Due to this ratio 2:1 for even/odd states, the two opposed quarter revival signals do not cancel completely each other, however, the signal has a reduced amplitude in comparison to the signal at the full and half revival times, as is observed in the experiment (Figure 4.5).

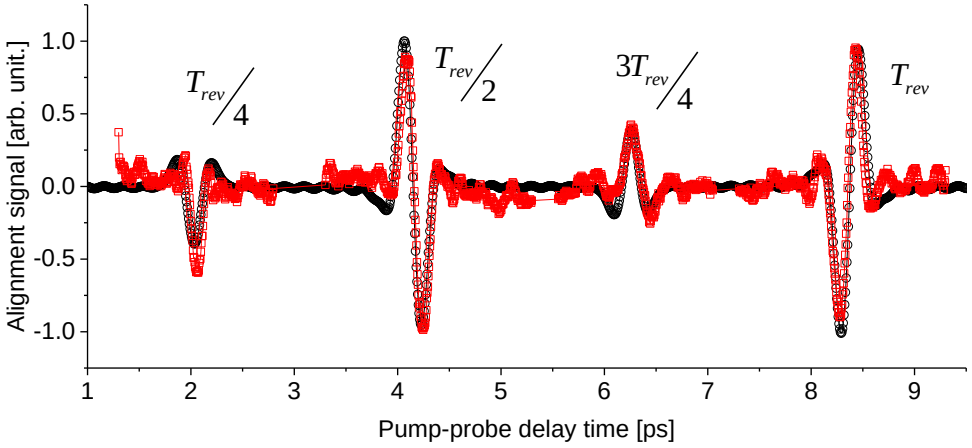

Figure 4.5 Molecular revivals of N_2 with initial temperature 300K. We use linearly polarized pump and probe pulses with peak intensities of $2\text{x}10^{13}$ W/cm^2 and $7.8\text{x}10^{13}$ W/cm^2, respectively. Red squares show experimental results and black circles depict calculated $\langle\langle\cos^2\theta\rangle\rangle$ parameter.

In Figure 4.6 we show the corresponding frequency spectrum of the time-dependent molecular alignment signal obtained from the Fourier transform (FT) in the case of N_2. The spectrum reveals two sequence as (6, 14, 22, 30, 38,…) *Bc* and (10, 18, 26, 34, 42, …) *Bc* due to allowed Raman transitions with the selection rule $\Delta J=\pm 2$ obtained from the matrix elements of $\left\langle\left\langle\cos^2\theta\right\rangle\right\rangle$. The sequence of each peak calculated as

$$(E_{J+2}-E_J)/2\pi=(4J+6)Bc=\begin{cases}6,14,22,30,38,46,54...\text{for even } J\\ 10,18,26,34,42,50,58...\text{for odd } J\end{cases}. \quad (4.3)$$

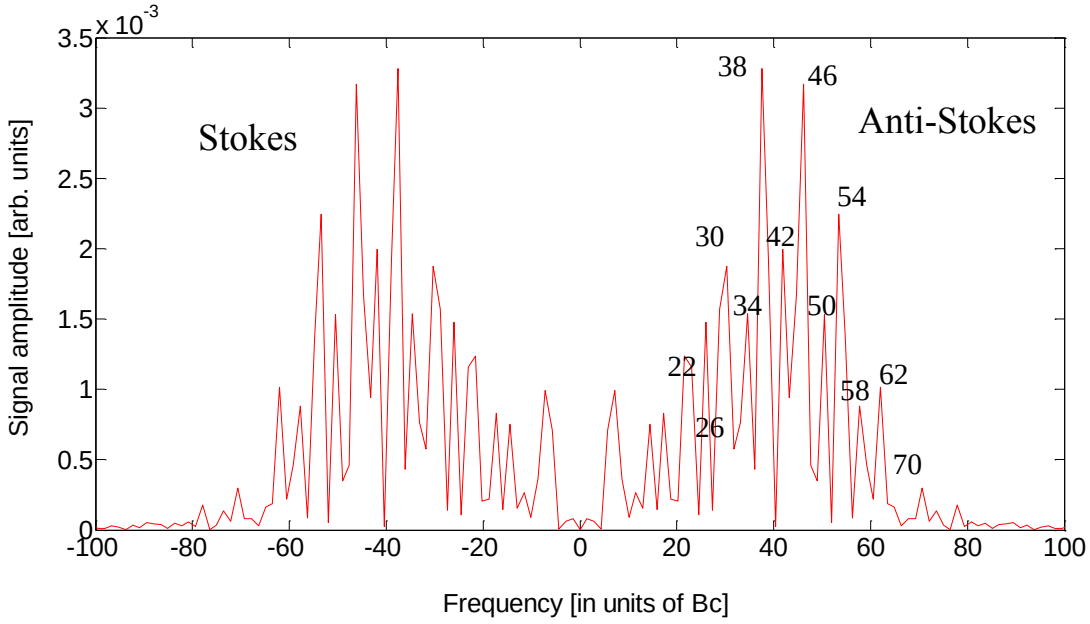

Figure 4.6 Frequency spectrum of the time-dependent molecular alignment signal shown in Fig. 4.5 signal for N_2. The number on each spectral peak shows the frequency in terms of $4J+6$ which corresponds with allowed Raman transitions. The series (6, 14, 22, 30, 38, 46, 54, …) *Bc* and (10, 18, 26, 34, 42, 50, 58, …) *Bc* come from even and odd values of *J*'s, respectively.

Recall that nuclear spin of nitrogen nucleus is 1 and both even and odd rotational states are permitted for nitrogen molecule. The relative ratio of even and odd states are found 2:1 considering nuclear spin statistics we explained earlier. Thus, the ratio 2:1 between the signal amplitude of the peaks seen in the frequency spectrum corresponding with even and odd J states can be understood with the same ratio obtained from nuclear spin statistics [36,86].

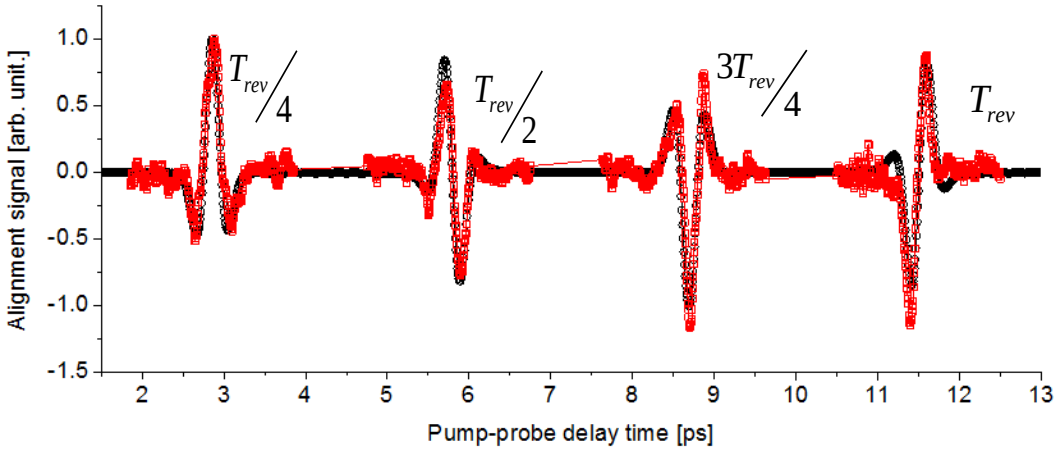

Figure 4.7 Molecular revivals of O_2 with initial temperature 300K. We use linearly polarized pump and probe pulses with peak intensities of $2x10^{13}$ W/cm^2 and $8.1x10^{13}$ W/cm^2, respectively. Red squares show experimental results and black circles present calculated <<$\cos^2\theta$>> parameter.

As presented in Figure 4.7 for oxygen molecule, we have observed wave packet revival signatures at quarter revival, half revival, three quarter revival, and full revival for O_2 molecules aligned by linearly polarized pump pulse, which agrees well with the calculated $\langle\langle \cos^2\theta \rangle\rangle$ alignment parameter. ^{16}O is a boson so the total wave function Ψ_{tot} is symmetric. The electronic wave function of ^{16}O, ψ_{el} , and the vibrational wave function, ψ_{vib} again correspond to the ground state. The ground state ($^3\sum_g^-$) of ψ_{el} for ^{16}O is antisymmetric [85], and therefore for Ψ_{tot} to be symmetric, $\psi_{r\,o}$ and ψ_{ns} must be

symmetric and antisymmetric or vice versa. For O_2 molecule the nuclear spin I=0 and only odd rotational states (J) are populated [87], and consequently the relative abundance of molecules with odd and even J is 1:0. Therefore, only a wave packet with odd J exists, and strong effects of alignment and anti-alignment are observed at the first and the three-quarter revivals of O_2 with the amplitude comparable to the full and half revival times, in agreement with the experiment (Figure 4.7).

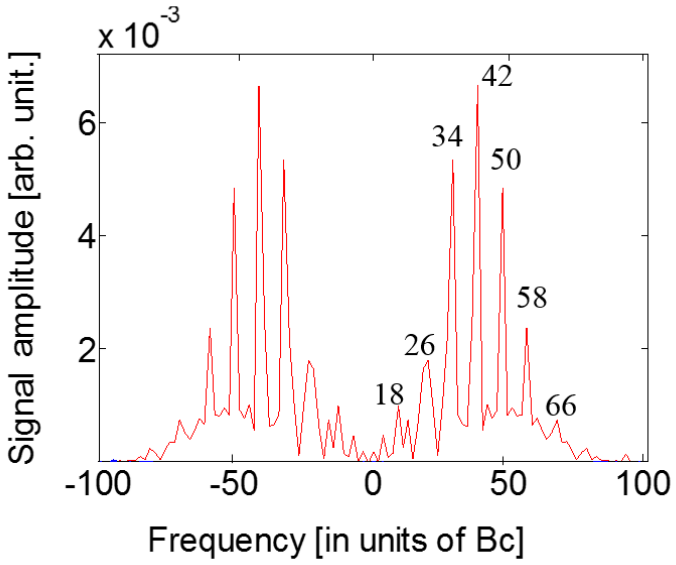

Figure 4.8 Frequency spectrum of the time-dependent molecular alignment signal shown in Fig. 4.7 signal for O_2. The number on each spectral peak shows the frequency in terms of $4J$+6 which corresponds with allowed Raman transitions given by the series (10, 18, 26, 34, 42, 50, 58, …) Bc for odd values of J.

In Figure 4.8, we show the corresponding frequency spectrum of the time-dependent molecular alignment signal obtained from the Fourier transform (FT) for O_2. The figure exhibits the experimental spectrum in prominent series as (10, 18, 26, 34, 42, …) *Bc*, since only odd *J* levels are permitted for O_2 due to the nuclear spin statistics.

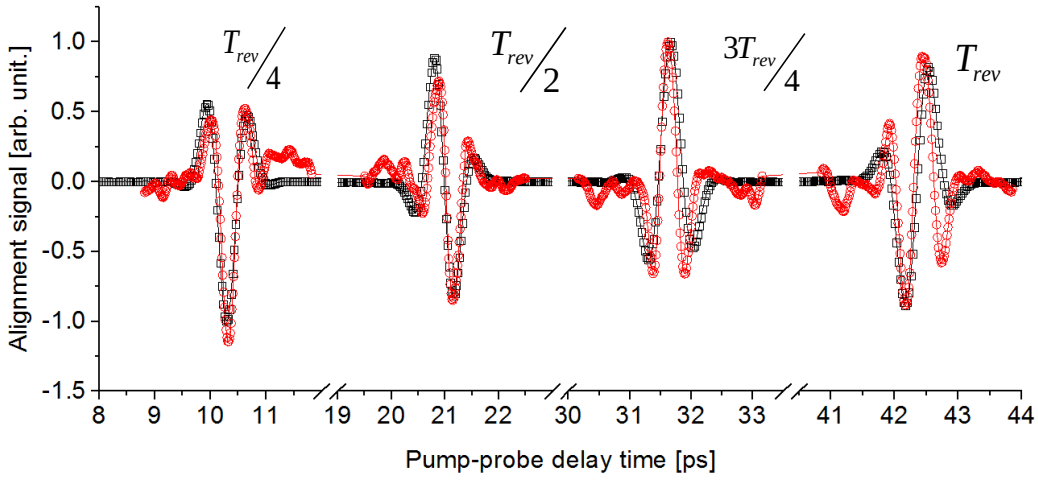

Figure 4.9 Molecular revivals of CO_2 with initial temperature 300K. We use linearly polarized pump and probe pulses with peak intensities of $1x10^{13}$ W/cm^2 and $7.6x10^{13}$ W/cm^2, respectively. Red squares show experimental results and black circles present $\langle\langle\cos^2\theta\rangle\rangle$ parameter.

Our experimental results for CO_2 are shown in Figure 4.9, where we presented wave packet revival signatures at quarter revival, half revival, three quarter revival, and full revival. These observations are in good agreement with the calculated $\langle\langle\cos^2\theta\rangle\rangle$

parameter. ^{16}O is a boson, so the total wave function Ψ_{tot} of CO_2 is symmetric. The ground electronic wave function, ψ_{el}, and vibrational wave function, ψ_{vib} ($^3\sum_g^+$) are symmetric, so for Ψ_{tot} to be symmetric ψ_{rot} and ψ_{ns} must be both symmetric or both antisymmetric. Two O atoms are identical, therefore the symmetric nature of the wave function demands that only even *J* states are populated [55,88]. Since only a wave packet with even *J* states exists, strong alignment signals are observed for carbondioxide molecule at $T_{rev}/4$ and $3T_{rev}/4$ revivals as seen in Figure 4.9.

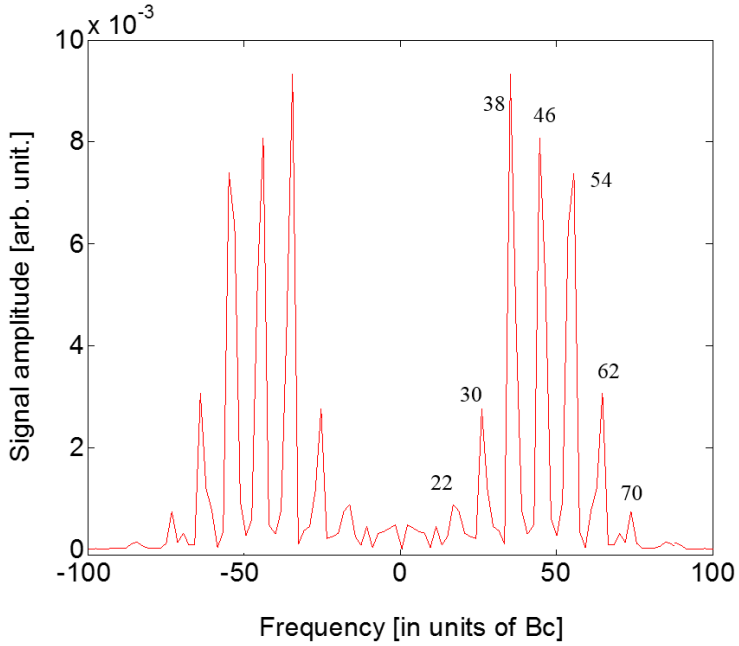

Figure 4.10 Frequency spectrum of the time-dependent molecular alignment signal shown in Fig. 4.9 signal for CO_2. The number on each spectral peak shows the frequency in terms of $4J+6$ which corresponds with allowed Raman transitions given by the series (6, 14, 22, 30, 38, 46, 54, …) *Bc* for even values of *J's*.

We also presented the corresponding frequency spectrum of the time-dependent molecular alignment signal obtained from the Fourier transform (FT) for CO_2. Only even *J* levels are permitted for CO_2 by the nuclear spin statistics so Figure 4.10 exhibits the experimental spectrum with series (6, 14, 22, 30, 38, 46, 54, …) *Bc* .

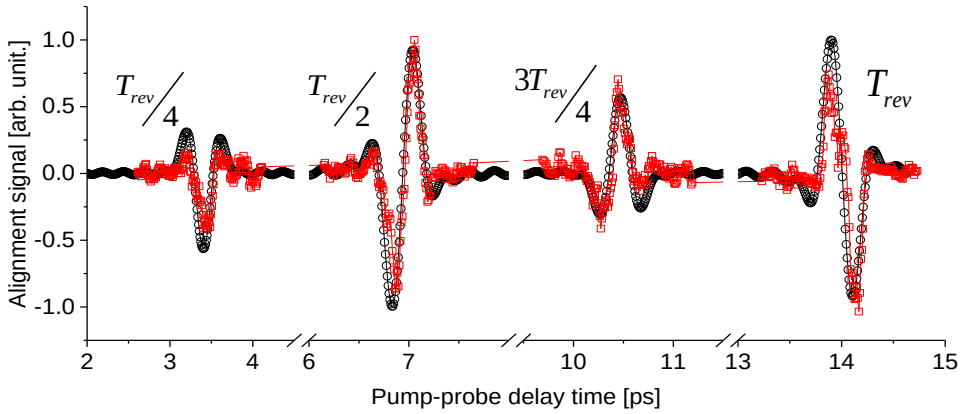

Figure 4.11 Molecular revivals of C_2H_2 with initial temperature 300K. We use linearly polarized pump and probe pulses with peak intensities of $3x10^{13}$ W/cm^2 and $7.6x10^{13}$ W/cm^2, respectively. Red squares show experimental data and black circles present calculated $<<\cos^2\theta>>$ parameter.

In the similar manner, one can conclude that acetylene C_2H_2 has both odd and even *J* states, which are populated with the ratio of odd J-states to even J-states 3:1 [87]. As a result of this fact, even and odd wave packets partially cancel each other and some alignment and anti-alignment are observed at quarter revivals as seen in Figure 4.11. We can clearly see that the result of molecular revivals of C_2H_2 molecules at quarter revival, half revival, three-quarter revival, and full revival are in good agreement with the calculated $\langle\langle \cos^2\theta \rangle\rangle$ parameter. The corresponding frequency spectrum of the time-dependent molecular alignment signal was obtained from the Fourier transform (FT) for

C_2H_2 as seen in Figure 4.12 The number on each spectral peak shows the frequency in terms of 4*J*+6 which corresponds with allowed Raman transitions given by the series (6, 14, 22, 30, 38, 46, 54, …) *Bc* for even values of *J*, (10, 18, 26, 34, 42, 50, 58, …) *Bc* for odd values of *J*. The relative ratio of the even over the odd can be understood as the 1:3 ratio of the nuclear spin statistics.

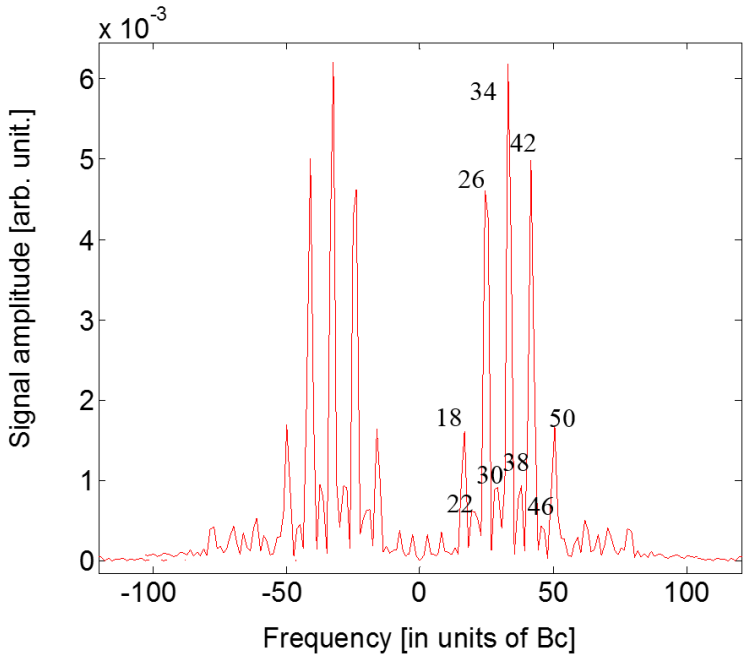

Figure 4.12 Frequency spectrum of the time-dependent molecular alignment signal shown in Fig. 4.11 signal for C_2H_2. The number on each spectral peak shows the frequency in terms of 4*J*+6 which corresponds with allowed Raman transitions given by the series (6, 14, 22, 30, 38, 46, 54, …) *Bc* for even values of *J*, (10, 18, 26, 34, 42, 50, 58, …) *Bc* for odd values of *J*. The relative ratio of the even over the odd can be understood as the 1:3 ratio of the nuclear spin statistics.

On the other hand, the CO molecule has nonidentical two nuclei. Because of this lack of symmetry, even and odd states in an ensemble of CO molecules are equally populated and the contributions come from even and odd rotational states completely cancel each other [78,89]. The main effect of this is that no quarter revivals appear in the time evolution of the alignment signal, as is shown in Figure 4.13. We observe only a half-revival and a full revival as is in the calculated $\langle\langle \cos^2\theta \rangle\rangle$ parameter in Figure 4.13. Frequency spectrum of the time-dependent molecular alignment signal for CO is expected to have peaks showing the frequency $4J+6$ as (6, 10, 14, 18, 22, 26, 30, 34, 38, 42, …) Bc for values of all J's (Figure 4.14).

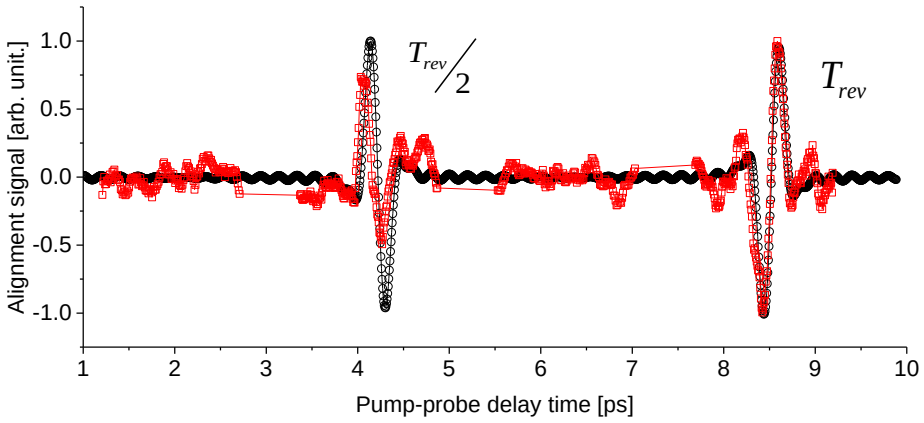

Figure 4.13 Molecular revivals of CO with initial temperature 300K. We use linearly polarized pump and probe pulses with peak intensities of $2\text{x}10^{13}$ W/cm^2 and $7.9\text{x}10^{13}$W/cm^2, respectively. Red squares show experimental data and black circles present calculated $\langle\langle\cos^2\theta\rangle\rangle$ parameter.

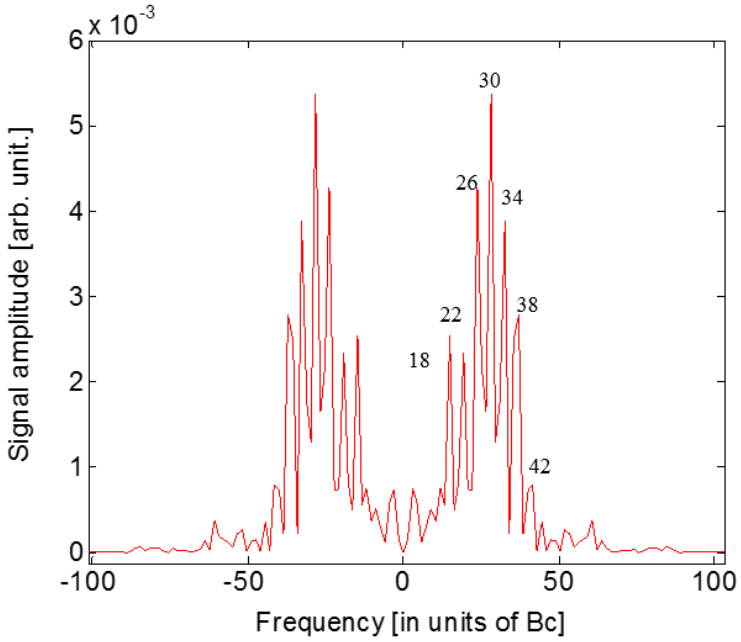

Figure 4.14 Frequency spectrum of the time-dependent molecular alignment signal shown in Fig. 4.13 signal for CO. The number on each spectral peak shows the frequency in terms of $4J+6$ which corresponds with allowed Raman transitions given by series (6, 10, 14, 18, 22, 26, 30, 34, 38, 42,…) *Bc*.

4.4.1.1 Determination of molecular rotational constants

We created fitting functions based on the Equation (2.30) of the alignment degree of the ensemble to determine the molecular rotational constants and revival times for each desired molecules. The determined molecular rotational constants and corresponding revival times for the selected molecules are presented in Table 2.

Table 2 Experimental and theoretical molecular rotational constants and corresponding molecular revival times [55,89-91]

	Rotational constants (cm^{-1})		Full Revival times (ps)	
	Experimental	Theoretical	Experimental	Theoretical
N_2	1.9994±0.004	1.9896	8.342	8.383
O_2	1.4611±0.022	1.4297	11.415	11.666
CO_2	0.3971±0.018	0.3902	42.000	42.743
CO	1.9393±0.004	1.9313	8.600	8.636
C_2H_2	1.1801±0.003	1.1766	14.133	14.175

4.4.2 Molecular alignment by circularly polarized pump pulses

We have also created rotational wave packets in a field-free condition using circularly polarized pump pulse for the linear molecules N_2, O_2, CO, and C_2H_2. To observe alignment signal, a delayed linearly polarized probe pulse was used to ionize the electrons in vacuum chamber. As we have explained in the Chapter II, in the case of dynamic alignment, aligning pulse gives a kick to the molecule, and applying a torque, rotate the molecular axis along the electric field polarization direction (xy) and then left the molecule by creating rotational wave packet in it. Due to the nature of quantum revivals, molecular wave packet realigns periodically to the plane of polarization every full revival period of the molecule.

The degree of molecular alignment is expressed as the expectation value of $\cos^2\theta$, $\left\langle\left\langle \cos^2\theta \right\rangle\right\rangle$. Theoretically, as we have already shown with the equations (2.23), (2.24), and (2.25); the matrix elements of $\left\langle\left\langle \cos^2\theta \right\rangle\right\rangle$ are the same for linearly and circularly polarized light. In addition, the Figure 4.15 shows simulation results that the alignment signal has reduced amplitude in the case of circularly polarized pump pulse in comparison to the linearly polarized pump pulse. Circularly polarized aligning (pump) pulse hits the molecules, first pulls the linear molecules into the polarization plane and this causes to decrease in the expectation value of alignment degree $\left\langle\left\langle \cos^2\theta_c \right\rangle\right\rangle$ at instant alignment [45].

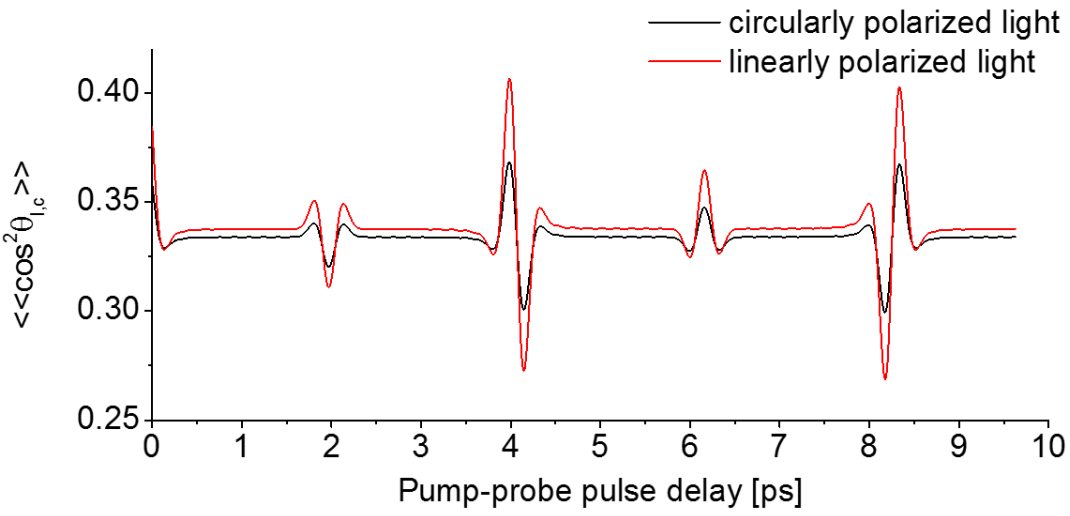

Figure 4.15 Calculated results of N_2 with linearly and circularly polarized light

The comparison between theoretical $\left\langle\left\langle \cos^2\theta_c \right\rangle\right\rangle$ and our experimental results are shown below for the molecules N_2, O_2, C_2H_2, and CO aligned by the circularly polarized pump pulse (Fig. 4.16-19). We measured photoelectron counts using variably delayed linearly polarized probe pulse. The electron yield depends on the probability of the aligned molecules along the probe pulse which ionized the electrons.

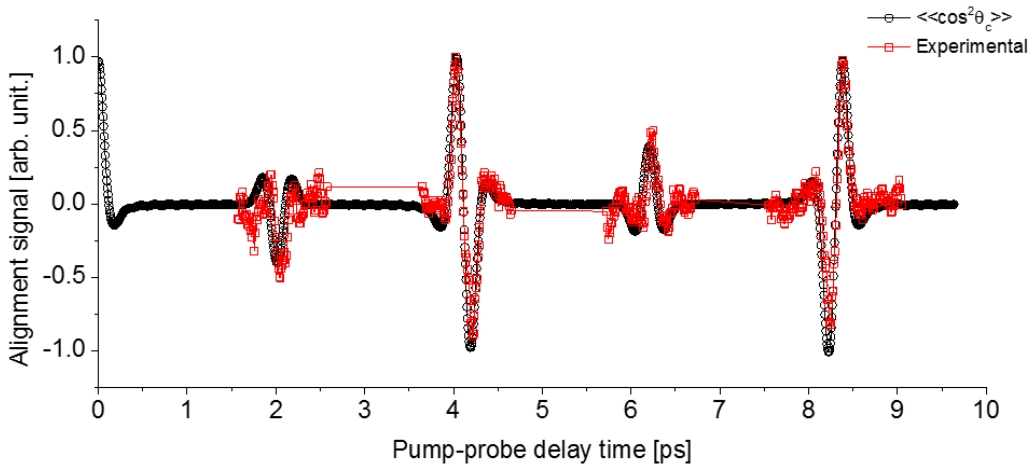

Figure 4.16 Molecular revivals of N_2 with initial temperature 300K. We use circularly polarized pump pulse with peak intensity of 2×10^{13} W/cm^2. Red squares show experimental results and black circles depict calculated $\langle\langle\cos^2\theta_c\rangle\rangle$

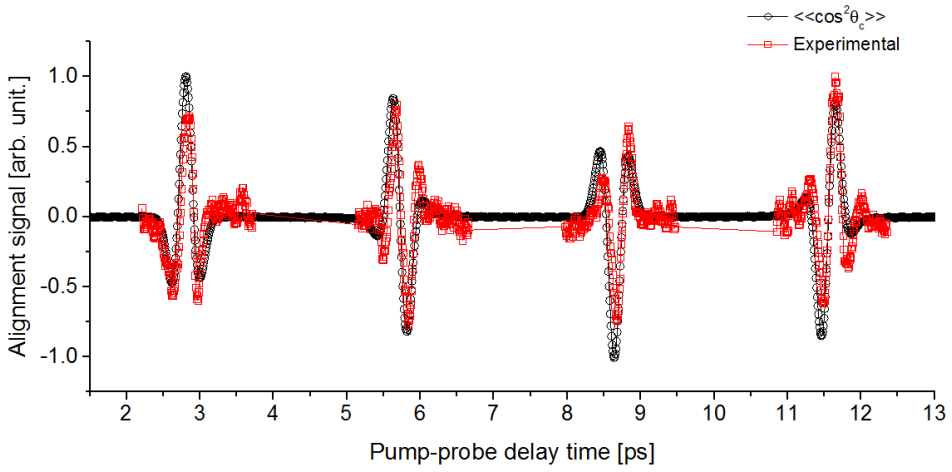

Figure 4.17 Molecular revivals of O_2 with initial temperature 300K. We use circularly polarized pump pulse with peak intensity of $2x10^{13}$ W/cm^2. Red squares show experimental results and black circles present calculated $<<\cos^2\theta_c>>$ parameter.

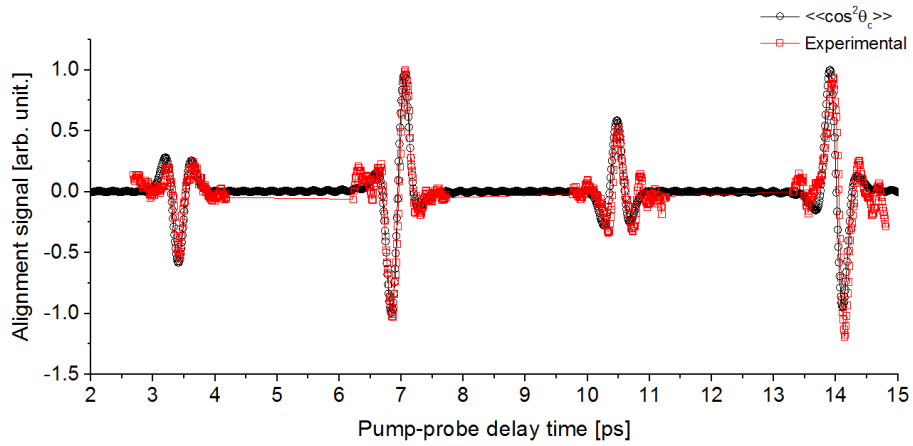

Figure 4.18 Molecular revivals of C_2H_2 with initial temperature 300K. We use circularly polarized pump pulse with peak intensity of $3x10^{13}$ W/cm^2. Red squares show experimental data and black circles present calculated $<<\cos^2\theta_c>>$ parameter

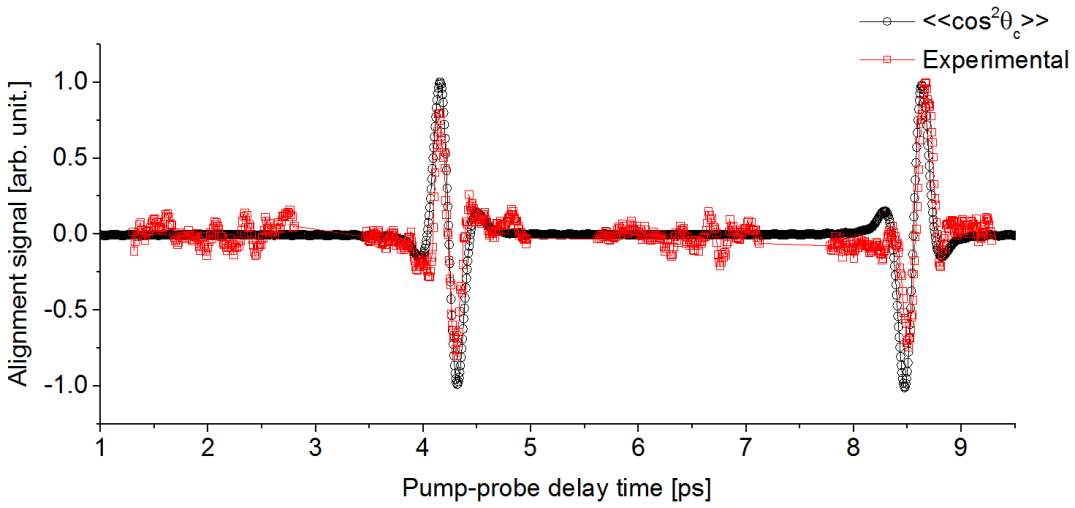

Figure 4.19 Molecular revivals of CO with initial temperature 300K. We use circularly polarized pump pulse with peak intensity of $3x10^{13}$ W/cm^2. Red squares show experimental data and black circles present calculated $<<\cos^2\theta_c>>$ parameter.

4.5 Conclusion

The revival signatures of linear molecules N_2, O_2, CO_2, CO, and C_2H_2 produced by linearly and/or circularly polarized pump pulse have been studied at a field-free alignment condition using detection of photoelectrons produced by a variably delayed probe pulse. Molecular dynamics of the linear molecules were studied by two different alignment conditions as linear and circular polarization and our experimental results were well fitted with the quantum mechanical calculations. Besides the measurement of the revival structures based on detection of photoelectrons, we also determined the molecular rotational constants by fitting our experimental values with our calculated results. The

measured revival structures and the rotational constants inferred from the measured data are in good agreement with the calculated results.

We have interpreted different wave packet evolutions of the linear molecules in terms of Highest Occupied Molecular Orbital (HOMO) and total nuclear spin of the molecule investigated. We observed strong alignment effects at multiples of $T_{rev}/2$ and reduced amplitude signals (not completely suppressed) at odd multiples of $T_{rev}/4$ due to the ratio of even:odd =2:1 for the spin-statistical factors of N_2. In the case of O_2 and CO_2, since only odd and only even *J* states are relevant, respectively, we observed the strong alignment signals for O_2 and CO_2 at $T_{rev}/4$ and $3T_{rev}/4$ revivals. In the case of a molecule like CO containing nonidentical nuclei, there is no additional factor arising from the nuclear spin statistics. Thus, the revivals at odd multiples of $T_{rev}/4$ are completely cancelled, whereas the revivals at multiples of $T_{rev}/2$ remain. For the C_2H_2, the corresponding ratio 1:3 can be expected so the observed strong alignment effects were at multiples of $T_{rev}/2$, and the reduced amplitude signals (not completely suppressed) were at odd multiples of $T_{rev}/4$.

HOMOs are the easiest place to donate electrons so we have to consider HOMO symmetry. Molecular ionization rate is supposed to be maximum when molecules are aligned along laser polarization direction for the molecules have maximum electron density along internuclear (molecular) axis such as nitrogen and carbonmonoxide due to σ_g and σ HOMOs, respectively, since they have no nodal plane along internuclear axis and it makes possible to eject electrons easily. Our experimental results for N_2 and CO

show that ionization rate is minimum just prior to the full revivals of each; and then in a short time ionization rate is maximum. On the other hand, our experimental result for C_2H_2 show that the ionization rate is maximum just prior to the full revival and then in a short time ionization rate is minimum which is opposite what we have observed for nitrogen and carbonmonoxide. Moreover, ionization rate dependency observed at the half revival is just reverse of what observed at the half revivals of nitrogen and carbonmonoxide. We can conclude that difference of the wave packet evolution is due to HOMO of acetylene which is π_u orbital. π_u molecular orbitals have electron density surrounding the bond axis (increased electron density above/below internuclear axis), with a node along the internuclear axis. Then, we can conclude the reverse structure of C_2H_2 with respect to the signals observed for N_2 and CO which have σ_g and σ HOMOs.

CHAPTER V

NONADIBATIC MOLECULAR ALIGNMENT MEASUREMENTS VIA WHITE-LIGHT GENERATION: QUANTUM CARPET OF MOLECULAR ALIGNMENT

The study presented in this chapter focuses on alignment of molecules by a short laser pulse and interaction of aligned molecules with filament. Initially, the topic will be given with the physics underlying the filamentation process. Then, we are going to detailed alignment-induced change of the refractive index. The experimental set up used will be presented to create laser-induced rotational wave packets in nitrogen and experimental procedure will be described to map the induced rotational wave packet as a function of the angular mismatch between polarization directions of femtosecond pump and probe pulses. The detailed experimental results will be compared with calculated results.

5.1 Introduction

Atomic and molecular media exposed to an intense and short femtosecond pulse show highly nonlinear dynamics leading to observations of phenomena such as high harmonic generation from filaments [92], long-range filament propagation [93], ultrashort pulse shaping and white-light generation [94,95], as well as wakes of molecular alignment [96]. The process of nonadiabatic molecular alignment occurs when a rotational wave packet is induced in non-symmetric molecules exposed to an ultrashort and intense laser pulse [72]. The nonlinear polarization exerted by a pump pulse yields an intensity-dependent refractive index and a transient birefringence as a result of the pulse interaction with a

molecular gas. Then a probe pulse propagates in the medium with properties that depend on the delay in the wake of the pump pulse. For certain conditions, the intense probe pulse can experience self-focusing and spatially collapse due to the dynamic Kerr effect. This collapse however stops when the intensity becomes high enough to generate free electrons and nonlinear losses tending to defocus the beam resulting in filamentary propagation [97]. The spatial and temporal characteristics of aligned molecules affect filamentation and white-light generation [98] so the latter process can be used as a probe to monitor the dynamics of molecular alignment. The studies of the molecular alignment in relation to filamentation have made progress in recent years [23,25,29,96,99-101]. It was shown that pre-aligned molecular gases can change the starting position of a filament [101] or increase the propagation distance of a filament [100]. The possibilities to control the length of two co-propagating filaments by creating molecular alignment [96] or a secondary filament emission, such as THz radiation [102,103] and supercontinuum generation [104], also were shown. In addition, the effect of molecular alignment on pulse compression [94] and its potential applications in attosecond physics were demonstrated [105,106].

In this study, we have used a filament as a probe to determine molecular dynamics of a non-ionized aligned medium. The degree of molecular alignment affects characteristics of the filament. By measuring the white-light from undergoing filamentation of the incident probe pulse after the ultrashort pump pulse has induced an alignment in nitrogen gas, we measured the rotational wave packet evolution of the gas. Then, by changing the angle between polarizations of the pump pulse and the filament-producing probe pulse and performing measurements for a range of pump-probe delays

around rotational revivals, we obtained a map of the rotational wave packet as a function of the polarization mismatch and delay between the pump and probe pulses, which is also known as a "quantum carpet" [107,108]. The experimental results from mapping rotational wave packets are compared with quantum mechanical calculations that follow Ref. [70].

5.2 Physics of filamentation

A medium experiences a spatiotemporal intensity dependent refractive index contribution due to the interaction with an intense electromagnetic field. Since the pulse shape is marked on the medium, considering a beam profile spatially and temporally Gaussian, the refractive index contribution is also Gaussian. The refractive index of the medium due to interaction with the laser beam is modulated as

$$n(r,t) = n_0 + n_2 I(r,t) \ , \tag{5.1}$$

where n_0 and n_2 are linear and second order refractive indices, respectively; and I is the intensity of propagating laser field. For most materials, the non-linear refractive index n_2 provides a positive contribution to the refractive index of the medium. If the phase shift originating from Kerr effect compensates the phase shift due to beam divergence self-focusing takes place. When the beam focuses, it triggers to increase of irradiance giving rise to stronger self-focusing. Once the ionization threshold is reached, it causes to

collapse of the material, leading to ionization. For the initial collapse, the self-focusing length of the beam with a Gaussian distribution of intensity [109] is determined as

$$L_{sf} = \frac{0.734\pi n_0 a_0^{\,2}}{\lambda_0\left[\left(\sqrt{P/P_{crit}} - 0.852\right)^2 - 0.0219\right]^{1/2}} , \tag{5.2}$$

where P is the power of the beam and a_0 is the radius of the beam profile at the 1/e level of intensity. The self-focusing length, L_{sf}, changes with the beam radius, a_0, and the ratio of the peak power over the critical power for self-focusing, P/P_{crit}.

The critical power of self-focusing is

$$P_{crit} = 3.77\frac{\lambda_0^2}{8\pi n_0 n_2} . \tag{5.3}$$

The generated plasma provides a negative focusing effect and the refractive index modification due to the plasma is [97]

$$n \simeq n_0 - \frac{\rho(r,t)e^2}{\omega_0^2 m_e \varepsilon_0} , \tag{5.4}$$

n is the plasma index of refraction, ρ is the electron density, e is the charge of an electron and m_e is the mass of an electron, ε_0 is the permittivity of the vacuum, and ω_0 is the central angular frequency of the laser beam. The main ionization processes play a role in the filamentation are multiphoton and tunnel ionization as described in Chapter IV.

The generation of plasma will defocus the laser beam and prevent from further self-focusing. The dynamic balance of the Kerr self-focusing and plasma defocusing clamps the maximum intensity (at a high intensity $\approx 5\times10^{13}\ \mathrm{W/cm^2}$) in a filament [110], see Figure 5.1.

Filamentation is a significantly nonlinear phenomenon and allows a variation of frequency generations to appear. Filamentation makes broader the spectrum of the pulse through processes self-phase modulation, ionization, and self-steepening [97]. Self-phase modulation originates from the temporal Kerr effect of self-focusing. An ultrashort pulse travelling in a medium leads to the change of the refractive index of the medium due to the Kerr-effect and this refractive index modification changes the frequency spectrum of the pulse. The refractive index of the medium depends on the temporal and spatial profile of the pulse. While the leading edge of the pulse generates red frequencies, trailing edge of the pulse generates blue frequencies in a normal dispersion Kerr medium. The spectrum will be chirped and broadened for a transform limited pulse.

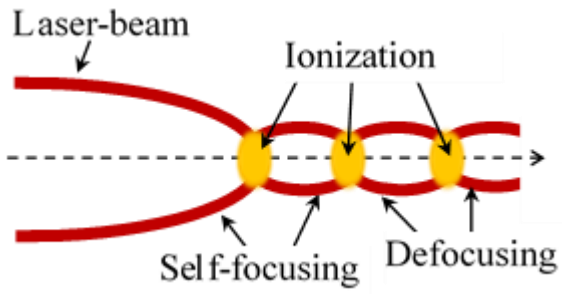

Figure 5.1 Filamentation dynamics.

Additionally, the multiphoton ionization influences the spectrum of the filamenting beam showing spectrally blue shifting of the spectrum [111]. Another process changes the spectrum of the filamenting beam is self-steepening. Self-steepening or the change of the pulse shape is observed because of the Gaussian pulse peak slowing with respect to the group velocity. This makes steeper the trailing edge of the pulse; enables the trailing edge of the pulse feel a stronger Kerr effect. Hence, it leads to generate blue frequencies more than red frequencies [112]. The nonlinear Kerr refraction index includes two components as the instantaneous electronic motion and nuclear/molecular response only for the molecules have anisotropic polarizability such as N_2 [99].

Briefly, filamentation is a nonlinear phenomenon depends on the linear and nonlinear refractive indices besides the induced ionization and the resulting plasma generation. We are going to examine dynamics of non-adiabatic molecular alignment through the filamentation process in the next section.

5.3 Description of an alignment-induced change of the refractive index

Here the theory will be presented to understand how refractive index changes depends on molecular alignment. When molecules with anisotropic polarizability experience aligning (pump) pulse in a non-adiabatic alignment condition, the refractive index changes both spatially and temporally. At first, we will describe change of refractive index considering the direction parallel to the field polarization. The dielectric response of gas molecules to the electric field applied is [113]

$$\varepsilon = n^2 = 1 + 4\pi N \langle \alpha \rangle (t) \ , \tag{5.5}$$

where n is the refractive index, N is the number of molecules, and $\langle \alpha \rangle (t)$ is the time-dependent ensemble average molecular polarizability along electric field of the laser. $\langle \alpha \rangle (t)$ is expressed as $\langle \alpha \rangle (t) = \langle \hat{\mathbf{e}} \cdot \alpha . \hat{\mathbf{e}} \rangle (t) = \langle e_i \alpha_{ij} e_j \rangle (t)$, where $\hat{\mathbf{e}}$ and α are the electric field polarization and the molecular polarizability tensor, respectively. Recall that the only nonvanishing components of polarizability tensor α are $\alpha_{zz} = \alpha_{\parallel}$ and $\alpha_{xx} = \alpha_{yy} = \alpha_{\perp}$ for a linear molecule, where the body-fixed z axis is selected along the molecular axis. We take the molecular symmetry along the z-axis, so the electric field of the laser can be considered as $\mathbf{E} = \hat{\mathbf{x}} E_x + \hat{\mathbf{z}} E_z$ for a particular molecular orientation. In the space-fixed field, for an ensemble of molecular orientations

$$n^2 = 1 + 4\pi N\left[\left\langle e_x^2\right\rangle(t)\alpha_{xx} + \left\langle e_z^2\right\rangle(t)\alpha_{zz}\right] = 1 + 4\pi N\left[\alpha_\perp\left\langle \sin^2\theta\right\rangle + \alpha_{\|}\left\langle \cos^2\theta\right\rangle\right] . \quad (5.6)$$

Then, it becomes

$$n^2(t) = 1 + 4\pi N\left[\Delta\alpha\left\langle \cos^2\theta\right\rangle(t) + \alpha_\perp\right] , \quad (5.7)$$

where $\Delta\alpha = \alpha_{\|} - \alpha_\perp$ and $e_z = \hat{\mathbf{e}}\cdot\hat{\mathrm{z}} = \cos\theta$ is the cosine of the angle between the electric field and the molecular axis (*z*).

The molecular ensemble before the pump pulse arrived is averaged over the solid angle and given by the expression

$$\left\langle \cos^2\theta\right\rangle(t = -\infty) = \frac{\int_0^\pi \cos^2\theta\sin\theta d\theta}{\int_0^\pi \sin\theta d\theta} = \frac{1}{3}. \quad (5.8)$$

Thus, linear refractive index is

$$n^2(t = -\infty) = n_0^2 = 1 + 4\pi N(\frac{1}{3}\Delta\alpha + \alpha_\perp) . \quad (5.9)$$

Then,

$$n^2(t) - n_0^2 = 4\pi N\left[\Delta\alpha\left(\left\langle\cos^2\theta\right\rangle(t) - \frac{1}{3}\right)\right]. \tag{5.10}$$

Since $n^2(t) - n_0^2 \ll n_0^2$, the index shift is given by

$$\Delta n_{\parallel}(t) = n(t) - n_0 = \frac{2\pi N}{n_0}\Delta\alpha\left(\left\langle\cos^2\theta\right\rangle(t) - \frac{1}{3}\right). \tag{5.11}$$

The degree of alignment of the ensemble at a rotational temperature T in thermal equilibrium $\left\langle\cos^2\theta\right\rangle(t)$ is written by averaging the degree of alignment of a single rotational state (2.27) over the Boltzmann distribution as $\left\langle\left\langle\cos^2\theta\right\rangle\right\rangle(t)$. Therefore, the nonadiabatic molecular alignment induces a periodic modulation of the change of refractive index of a gas along the polarization direction of the aligning pulse which is given by [21]

$$\Delta n_{\parallel}(r,t) = n(t) - n_0 = \frac{2\pi N}{n_0}\Delta\alpha\left(\left\langle\left\langle\cos^2\theta\right\rangle\right\rangle(r,t) - \frac{1}{3}\right), \tag{5.12}$$

where $\left\langle\left\langle \cos^2\theta \right\rangle\right\rangle(r,t)$ is the thermally averaged alignment expectation value as described in Eq.(2.30).

On the other hand, the change in the refractive index considering the direction perpendicular to the field polarization is described by [114-116]

$$\Delta n_{\perp}(r,t) = -\frac{1}{2}\Delta n_{\parallel}(r,t) = -\frac{\pi N}{n_0}\Delta\alpha\left(\left\langle\left\langle \cos^2\theta \right\rangle\right\rangle(r,t) - \frac{1}{3}\right), \tag{5.13}$$

assuming that the plasma has inclination neither parallel nor perpendicular to the field polarization of the laser [117,118]. Then the resulting birefringence, the nonlinear refractive indices difference $\Delta n(r,t)$, can be expressed as [96,113,119]

$$\begin{aligned}\Delta n(r,t) &= \Delta n_{\parallel}(r,t) - \Delta n_{\perp}(r,t) \\ &= \frac{3\pi N}{n_0}\Delta\alpha\left(\left\langle\left\langle \cos^2\theta \right\rangle\right\rangle(r,t) - \frac{1}{3}\right),\end{aligned} \tag{5.14}$$

i.e., the change of the refractive index is proportional to the deviation of the alignment degree from the isotropic one, which equals to 1/3.

The self-phase modulation, arising from the intensity dependence of the refractive index, can cause a spectral broadening of the pulse and consequently the white-light generation. When an optical field experiences the self-induced intensity-dependent

nonlinear phase shift during its propagation in a Kerr medium, this phase shift is given by [120,121]

$$\phi_{NL}(t) = -\Delta n(t)\,\omega_0 L/c\,, \tag{5.15}$$

where t is time delay between pump and probe pulses, Δn is the change in the refractive index due to the electronic Kerr cross-phase modulation, the plasma formation, and the molecular alignment, ω_0 is the central angular frequency, L is the length of the Kerr medium, and c is the speed of light. Then, considering the polarization of the pump pulse is in the x direction and the propagation is in the z direction, for each polarization of the probe pulse, the modulation of the refractive index due to the electronic Kerr effect is given by the expression [120,122,123]

$$\Delta n_{Kerr,x}(t) = 2n_2 I_{pump}(\mathrm{t}) \tag{5.16}$$

and

$$\Delta n_{Kerr,\mathrm{y}}(t) = \frac{1}{3}\Delta n_{Kerr,\mathrm{x}}(t). \tag{5.17}$$

The plasma contribution to the refractive index is given by [124]

$$\Delta n_{plasma}(t) = -\frac{2\pi e^2 N_e(t)}{m_e \omega_0^2}\,, \tag{5.18}$$

where ω_0 , $N_e(t)$, e, and m_e are the central angular frequency of the laser, electron density, charge of an electron, and mass of an electron, respectively. The pump had intensity too low to produce a filament so the electronic Kerr effect and plasma formation have been neglected and we can only consider the refractive index changes caused by the molecular alignment. On the other hand, alignment produces a noticeable change in filament formation and white-light generation when the amplitude of the change of the refractive index due to alignment $\Delta n_{align} = \Delta n(\mathbf{r}, t)$ produced by the pump beam becomes comparable to the refractive index change owing to the optical Kerr effect, $\Delta n_{Kerr} = n_2 I_{probe}$, induced by the probe beam with intensity I_{probe}. With $n_2(N_2) = 2.3\times10^{-19}\,\mathrm{cm}^2/\mathrm{W}$ and $I_{probe} = 5\times10^{13}\,\mathrm{W/cm}^2$, we obtain $\Delta n = 4.4\times10^{-5}$ for a typical gas pressure of 4 bar. A similar value of the magnitude of the refractive index variations due to alignment Δn_{align} follows from calculations of the pump pulse with intensity $I_{pump} = 10^{13}\,\mathrm{W/cm}^2$ and duration $\tau \approx 250\,fs$, which fits well with experimental parameters. The additional contribution to the alignment, caused by the alignment, changes the self-focusing length: it decreases for alignment and increases for anti-alignment, thus the dynamics of the rotational wave packet changes the filament formation and modulates the white-light generation.

Note that nonlinear optical processes such as self-phase modulation (SPM) affects the temporal phase and causes some changes of the frequency spectrum of the laser pulse. The frequency shift due to SPM is given by

$$\delta\omega(t) = \frac{d}{dt}\phi_{NL}(t) = -\frac{d}{dt}\Delta n(t)\,\omega_0 L/c, \tag{5.19}$$

which corresponds to

$$\Delta\lambda \approx \frac{L\lambda_0}{c}\frac{d}{dt}\Delta n(t) \tag{5.20}$$

in the wavelength domain, assuming the limit of small spectral shifts $\Delta\lambda \ll \lambda_0$ [121]. As it is presented, $\delta\omega(t)$ accounts only for the broadening due to modulation of the refractive index by the rotational wave packet evolution. Since the time scale of these changes is related to revivals, it is about 200fs and quite large. The steepening on the scale of an optical period (~2.6 fs) (self-phase modulation) can give larger changes of the wavelength.

5.4 Experimental procedures

Our experiments were done with a Ti:sapphire amplified laser system which has a pulse duration of ~50 fs, central wavelength of 800 nm, and an output energy of 1 mJ per pulse at a 1 kHz repetition rate. A laser beam is split into two parts by a beam splitter (BS) to obtain the pump and probe pulses with a specific ratio of intensity between them as shown in Figure 5.2. The probe pulse is then delayed with a controllable delay line system. The

delay time of the probe pulse with respect to the pump pulse was precisely adjusted using an optical variable time delay with a translational stage controlled by a stepping motor (GTS150, ESP301, Newport). We used a combination of beam polarizer and half or quarter wave plate for adjusting the intensity of the pump beam. When needed, it was used with a polarizer to set the beam power to be the same for all polarization angles. This was achieved by controlling two Picomotor rotary stages with a Picomotor drivers and adapters (New Focus, Model 8701). The two pulses with a relative delay were then recombined with another beam splitter, the pump pulse polarization could be rotated with respect to that of the pump pulse by an arbitrary angle α. Then, the recombined beams were focused using a focal length of f=60 cm lens into a sealed gas cell with 85 cm length, which was filled with 99.9995% purity N_2 from Matheson TRIGAS to a maximum pressure of 4 atm, which was preceded by evacuating the gas cell down to $2x10^{-3}$ mbar. The pump pulse was adjusted to have an intensity too low to produce a filament but aligned the molecules so the electronic Kerr effect and the plasma can be negligible for pump pulse interaction with molecules in alignment purposes. The intensity of the probe pulse at the focus was set to $\approx 5\times10^{13}\,\mathrm{W/cm^2}$ (the dynamic balance of the Kerr self-focusing and plasma defocusing clamps the maximum intensity in a filament just at about the same value [110]) to observe and measure alignment produced by the probe pulse using white-light generation. By blocking the probe pulse, we made sure that no white-light is generated with pump pulse only. We compared theoretical calculations of nonadibatic alignment with experimental measurements of white-light production. We determined the acceptable experimental tolerances for the alignment dynamics in such a way that we saw it did not cause a

significant change in the outcomes by making small changes in pressure ± 0.1 bar and intensity of the alignment pulse ~20% difference in intensity.

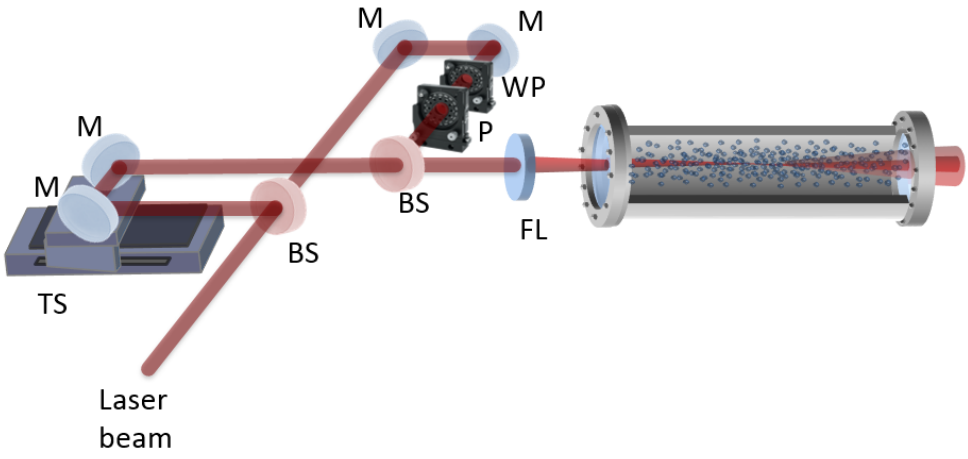

Figure 5.2 The schematic of the experimental setup. BS: beam-splitters, TS: translational stage, WP: wave plate, P: polarizer, M: flat mirrors, and FL: focusing lens.

At the exit of the gas cell, the white-light signals, spectral profiles, and durations of the pulses were measured simultaneously by reflecting a small portion of the beam with a beam splitter positioned after the cell. In the spectral measurements, the radiation collected in an integration cavity was measured by an Ocean Optics USB-2000 spectrometer. Simultaneously, power measurements were performed using a photodiode power meter head (Ophir PD300-UV) with a spectral range within 200-1100 nm. The pulse duration measurements were taken with the Grenouille (8-20, Swamp Optics). We automated the experiments using National Instruments (NI) DAQ PCI-MIO-16E-4 card,

NI BNC 2090 box and custom NI LabView programs. The Newport ESP301 (for pump-probe delay) and a set of New Focus rotary stages with pico-drivers and adapters (the holder for waveplate and polarizer combination to rotate beam polarization and also set the beam power the same for all polarization angles), Ocean Optics USB2000, OPHIR NOVA II power meter, and the Grenouille (8-20, Swamp Optics) were automated by Labview sub-VI's and incorporated into a Labview VI program that controlled the entire experiment and data collection. The measured white-light was spectrally filtered to remove the IR radiation (λ>650nm) of the pump and probe beams (Figure 5.3).

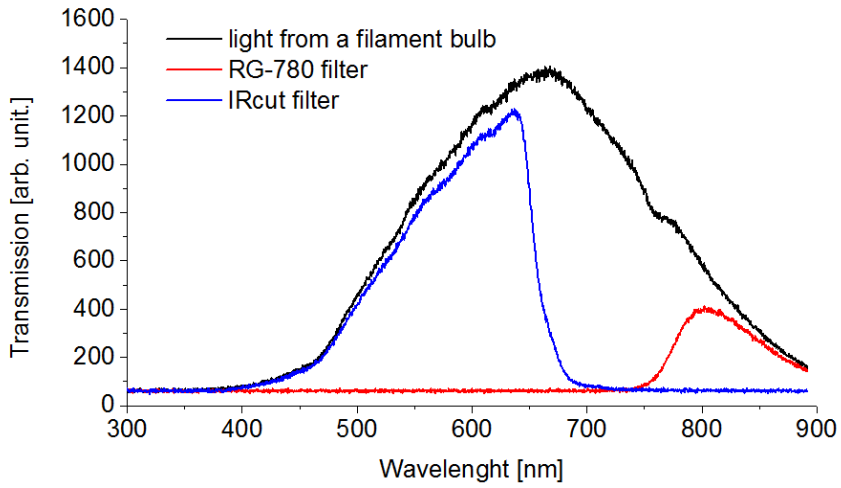

Figure 5.3 Optical filters selectively transmitted light having certain a particular range of wavelengths.

5.5 Results and discussion

5.5.1 Molecular alignment observation with parallel polarizations of pump and probe pulses

Figure 5.4 shows the experimental molecular alignment results in nitrogen gas at 300K compared to the calculated alignment-induced change of the refractive index, $\left\langle\left\langle \cos^2\theta \right\rangle\right\rangle - 1/3$. The alignment was monitored by measuring the power of white-light generated by the delayed probe pulse. When the probe pulse field polarization is oriented parallel with molecular axes (parallel molecular alignment) a positive change of the refractive index is induced. When the probe pulse field polarization is perpendicular to the axes of molecules (perpendicular molecular alignment) a negative change of the refractive index is created. Since the beam mode is close to Gaussian, it is expected that the alignment is stronger in the beam center. Since the beam mode is close to Gaussian, it is expected that the alignment is stronger in the beam center. Accordingly, at parallel molecular alignment revivals a spatial focusing of the probe beam was induced while for perpendicular molecular alignment revivals spatial defocusing took place. Consequently, for additionally focused probe pulse, the peak intensity increased and self-focusing developed faster, which should result in enhancing the white-light generation while defocusing should result in a decrease of the white-light output. Indeed, we observed the enhancement of the white-light generation for molecular alignment parallel to the probe pulse polarization direction, while for the alignment perpendicular to the polarization direction the white-light generation was suppressed.

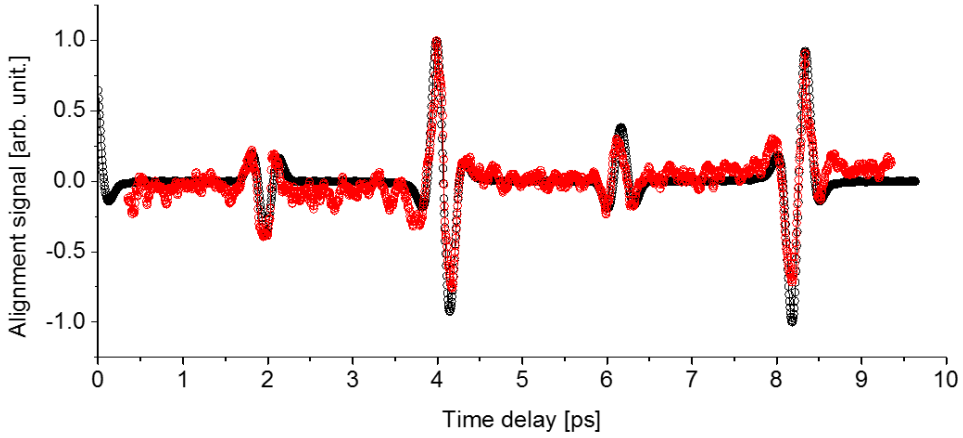

Figure 5.4 Comparison of the temporal evolution of the theoretical nonlinear refractive index (black circles) and experimental measured white-light generation (red circles) in nitrogen gas at 300 K during molecular alignment with variation of the delay between the pump and probe pulses. We use a linearly polarized pump and probe pulses with peak intensities of $2x10^{13}W/cm^2$ and $5x10^{13}W/cm^2$, respectively.

For interpretation of the results we will consider the total wave function of the linear molecule, which according to the Born-Oppenheimer approximation can be factorized $\Psi_{tot} = \psi_{el} \times \psi_{vib} \times \psi_{rot} \times \psi_{ns}$, as a product of the electronic wave function ψ_{el}, the vibrational wave function ψ_{vib}, the rotational wave function ψ_{rot}, and the nuclear spin wave function ψ_{ns}, as discussed in Chapter II. According to the nuclear spin statistics of $^{14}N_2$, for this molecule the total wave function Ψ_{tot} is symmetric [12]. The electronic wave function of ^{14}N, ψ_{el} $(^3\sum_g^+)$, and the vibrational wave function, ψ_{vib} corresponding to the

ground state are also both symmetric [85]. Therefore, to understand ψ_{rot} behavior, we should consider symmetric and antisymmetric forms of nuclear spin wave function ψ_{ns} of the nitrogen molecule. For Ψ_{tot} to be symmetric both ψ_{rot} and ψ_{ns} must be symmetric or antisymmetric. The nuclear spin of ^{14}N is I=1 and the total nuclear spin of the molecule can take only values I_{tot}=0, 1, or 2, and consequently N_2 has even (I_{tot}=0, 2) and odd (I_{tot} =1) values. For a state with total nuclear spin I_{tot} the degeneracy is 2 I_{tot} +1, and then the statistical weights of even-N_2 and odd-N_2 are 6 and 3, respectively. Thus, the relative ratio of even-N_2 versus odd-N_2 is 2:1 [36]. Due to this ratio for even/odd states, the two opposed quarter revival signals do not completely cancel each other, however, the corresponding signals have reduced amplitudes in comparison to the signals at the full and half revival times, as is obtained in the experiment and quantum mechanical calculations (Figure 5.4).

In Figure 5.5 we show the corresponding frequency spectrum of the time-dependent molecular alignment signal obtained by the Fourier transform (FT) in the case of N_2. The spectrum reveals two sequence as (6, 14, 22, 30, 38,…)Bc and (10, 18, 26, 34, 42,…)Bc. Recall that the only nonzero matrix elements of $\left\langle\left\langle \cos^2\theta \right\rangle\right\rangle$ are ΔJ=0, ±2 and allowed Raman transitions satisfy the selection rule ΔJ=±2. Because nuclear spin of nitrogen nucleus is 1, both even and odd rotational states are permitted for nitrogen molecule. Then, the sequence of spectral peaks can be calculated as $(E_{J+2} - E_J)/2\pi = (4J+6)Bc$ as 6, 14, 22, 30, 38, … for even J's and 10, 18, 26, 34, 42, … for odd J's. The observed larger amplitudes of the peaks seen in the frequency spectrum for the even J-states compared to the odd J-states qualitatively corresponds to

the ratio 2:1 between the populations of the even and odd *J*-states following from the nuclear spin statistics [36,49,86].

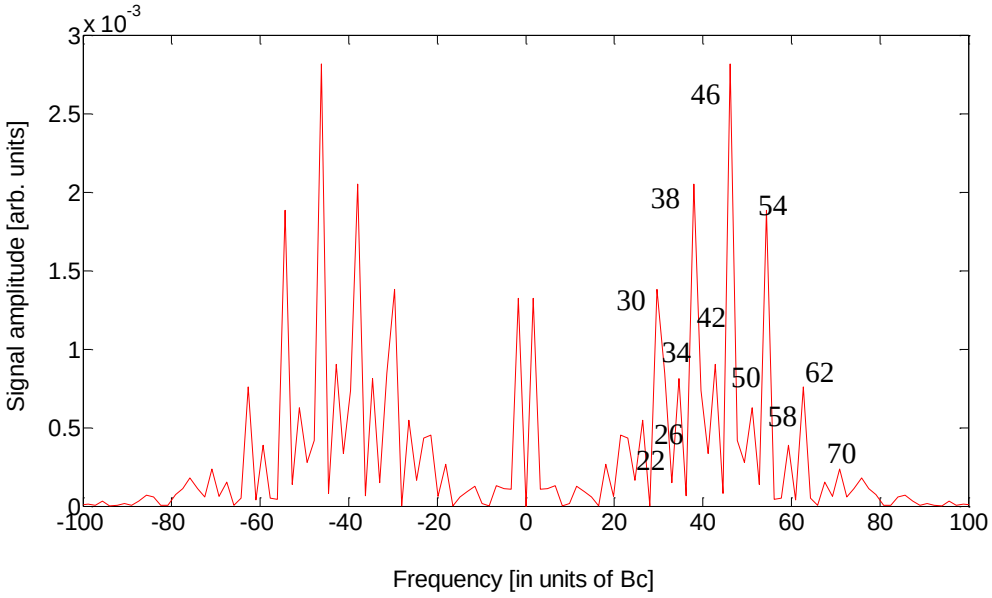

Figure 5.5 Frequency spectrum of the time-dependent white-light generation (alignment signal) shown in Fig. 5.4 for N_2. The number on each spectral peak shows the frequency in terms of $4J+6$ which corresponds with allowed Raman transitions given by the series (6, 14, 22, 30, 38, 46, 54, …) *Bc* for even values of *J*, (10, 18, 26, 34, 42, 50, 58, …) *Bc* for odd values of *J*. The peaks near zero are an artifact.

Simultaneously with the output power measurements of the white-light, we have also measured changes of the pulse duration of the probe pulse after it propagated through the gas cell, as shown in Figure 5.6. As presented in Figure 5.6, enhancement in filamentation causes a shortening of the pulse duration. At the minimum of the rotational

revivals, the pulse duration become becomes broadened due to the effect of chromatic dispersion in the gas on the propagating pulse. The measured average pulse duration 140fs substantially exceeding the initial 50fs pulse duration accounts for the dispersion in gas cell and the entrance and exit glass windows. Therefore, we correlated our pulse measurement with the self-induced intensity-dependent nonlinear phase shift $\phi_{NL}(t) \propto -\Delta n(t)$ as a function of the delay time *t* between the pump and probe pulses. The pulse duration modifications were observed about ± 10fs at the revival signatures of molecular alignment.

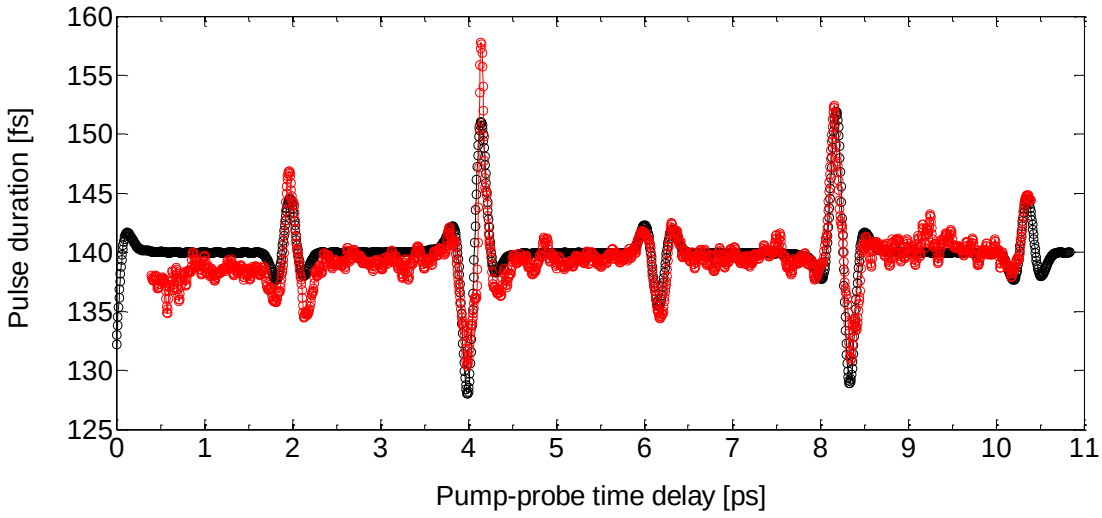

Figure 5.6 Comparison of experimentally measured temporal evolution of the pulse duration (red circles) induced by molecular alignment evaluated by white-light signal measurement and corresponding pulse duration calculations (black circles) for different relative delays between the pump and probe pulses.

We also measured the spectral changes dependent on the revival events induced by molecular alignment and evaluated by filamentation signal measurement for different relative delays between the pump and probe pulses as seen in Figure 5.7. After the aligning pump pulse propagate in the air, the molecules in the air experience revival events periodically in the nonadiabatic alignment condition. The following pulse undergoes spectral broadening at the maxima of the rotational revivals of the molecules.

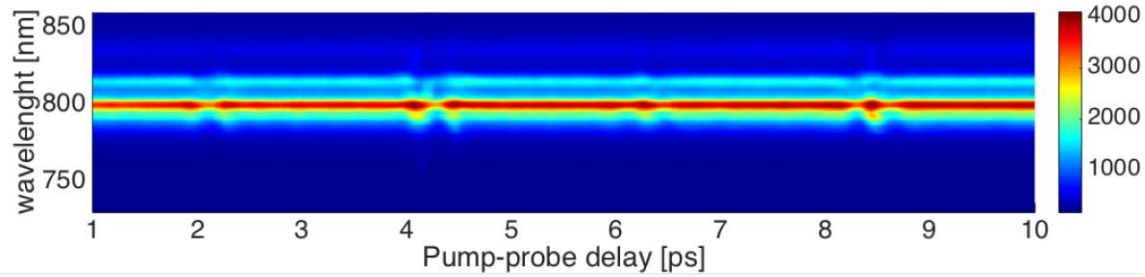

Figure 5.7 Spectral changes dependent on the revival events induced by molecular alignment and evaluated by filamentation signal measurement for different relative delays between the pump and probe pulses.

So far we have considered that the polarizations of the pump and probe pulses are parallel. We have demonstrated that white-light generation reflects the processes of molecular alignment. The probe pulse propagating in the alignment wake of the pump pulse experiences variations of the refractive index and, as a result, its duration and spectrum are also modulated by revivals.

5.5.2 Molecular alignment observation with arbitrary orientations of pump and probe polarizations

In this section we will consider molecular alignment with arbitrary mutual orientation of polarizations of the pump and probe pulses. We may define the relative angle between the polarizations of pump and probe pulses, α , to lie in the xy plane (see Figure 5.8). The expectation value of the alignment [47] for an arbitrary angle α is given by

$$\left\langle\left\langle \cos^2\theta' \right\rangle\right\rangle = \frac{1}{2}\left(3\cos^2\alpha - 1\right)\left\langle\left\langle \cos^2\theta \right\rangle\right\rangle(t) + \frac{1}{2}\sin^2\alpha \tag{5.21}$$

where $\left\langle\left\langle \cos^2\theta \right\rangle\right\rangle(t)$ is the thermal averaging of the degree of alignment (see Eq. (2.30)) and θ' is the angle between molecular axis and polarization of the pump beam.

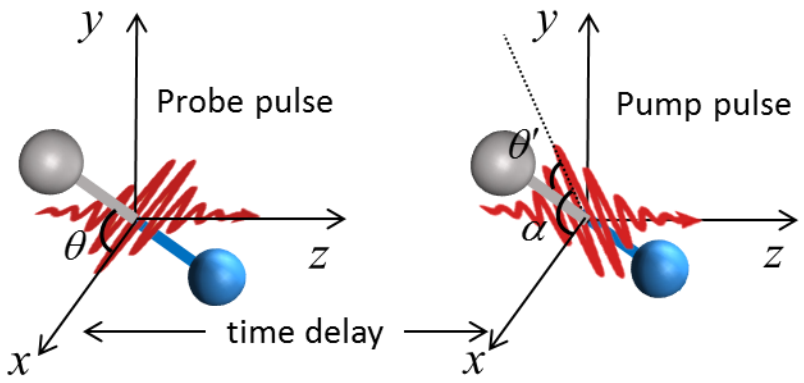

Figure 5.8 A schematic diagram defining molecular axis, α is the angle between pump and probe polarization in xy plane. The fields are assumed to propagate along the z-axis.

For the parallel polarization $\alpha = 0$ we have $\left\langle\left\langle \cos^2\theta' \right\rangle\right\rangle = \left\langle\left\langle \cos^2\theta \right\rangle\right\rangle(t)$ and for the perpendicular polarization $\alpha = 90^\circ$, $\left\langle\left\langle \cos^2\theta' \right\rangle\right\rangle = \frac{1}{2}\left[1 - \left\langle\left\langle \cos^2\theta \right\rangle\right\rangle(t)\right]$, which has obviously opposite phase as a function of t for the full revival of N_2 as seen in Figure 5.9.

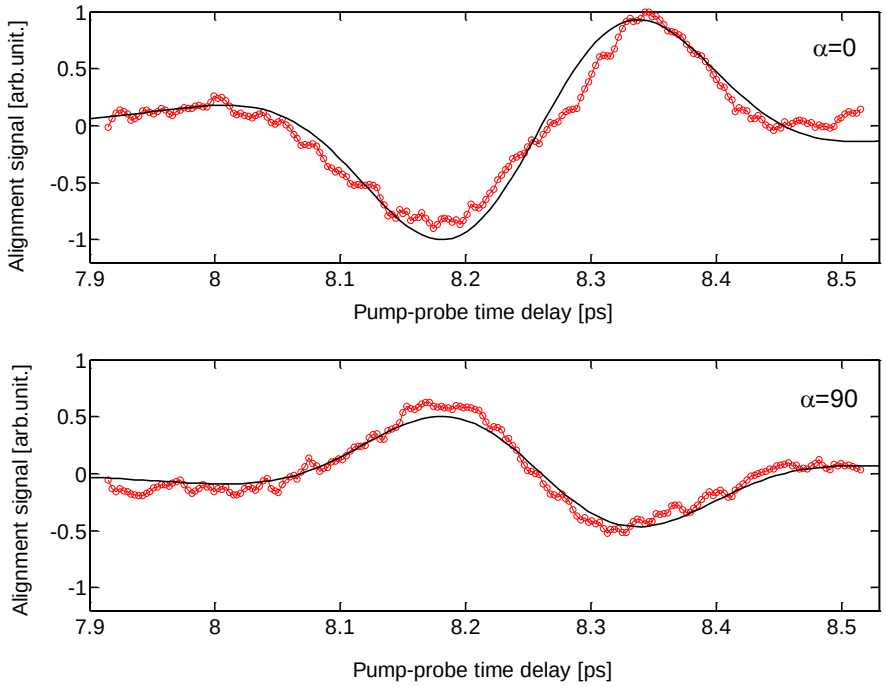

Figure 5.9 Full revival of N_2 for pump-probe polarizations parallel, α=0°, and perpendicular, α=90°. Red circles depict the measured white-light power, and the black solid line shows the calculated nonlinear refractive index change. The data was normalized to the magnitude of the parallel polarization signal.

Indeed, at $\alpha = 0^{\circ}$ the full revival signal shows a minimum around 8.2ps (anti-alignment) and a maximum around 8.35ps (maximal alignment) while at $\alpha = 90^{\circ}$ the full revival shows a maximum around 8.2ps (maximal alignment) and a minimum (anti-alignment) around 8.35ps. We can also see that the modulation depth for α=90° is smaller than the one for α=0°. In addition, the measured molecular alignment degree of the revival with perpendicular polarizations was about half of the one with parallel polarizations, which is consistent with the fact that $\left\langle\left\langle \cos^2\theta_{\parallel}\right\rangle\right\rangle + 2\left\langle\left\langle \cos^2\theta_{\perp}\right\rangle\right\rangle = 1$.

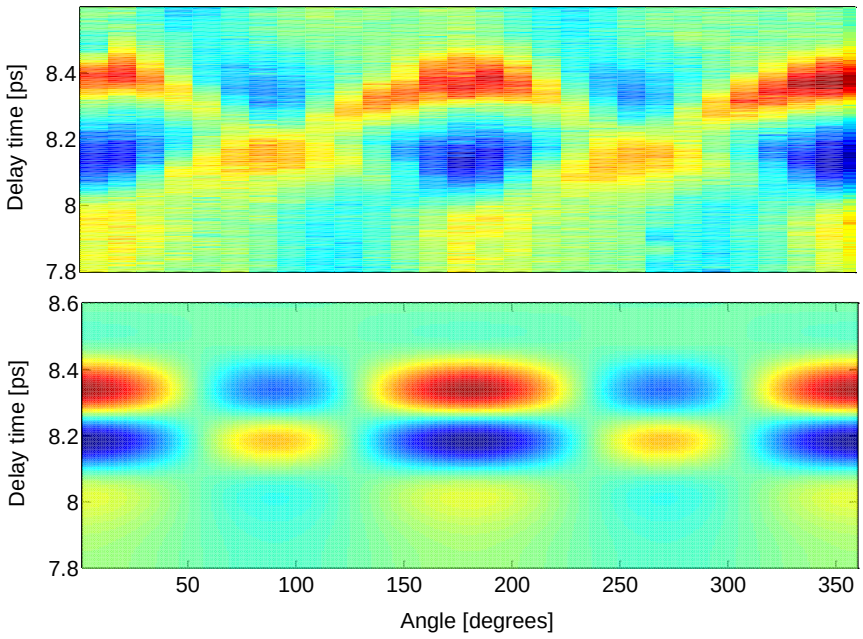

Figure 5.10 Experimental (top) and theoretical (bottom) quantum carpets of a rotational full revival around 8.3ps.

In order to investigate how the structure of the rotational full revival changes with polarization angle α, we ran the experiment for a series of pump-probe scans with different pump pulse polarization angles. The rotational wave packet evolution of the full revival was mapped for a range of pump-probe delays by rotating the pump pulse polarization with respect to the horizontally polarized probe pulse; the resulting structure is the so-called "quantum carpet" [107]) shown in Figure 5.10. The theoretical results are calculated by using Eq.(5.21). As can be seen from the calculated quantum carpet in Figure 5.10, there is an angle at which the expectation value of the alignment is the same for all delay times. This angle, as follows from Eq.(5.21), is given by $3\cos^2\alpha_c - 1 = 0$, i.e. $\alpha_c \approx 55°$. We can see that this conclusion agrees well with our experimental data, given in Figure 5.10.

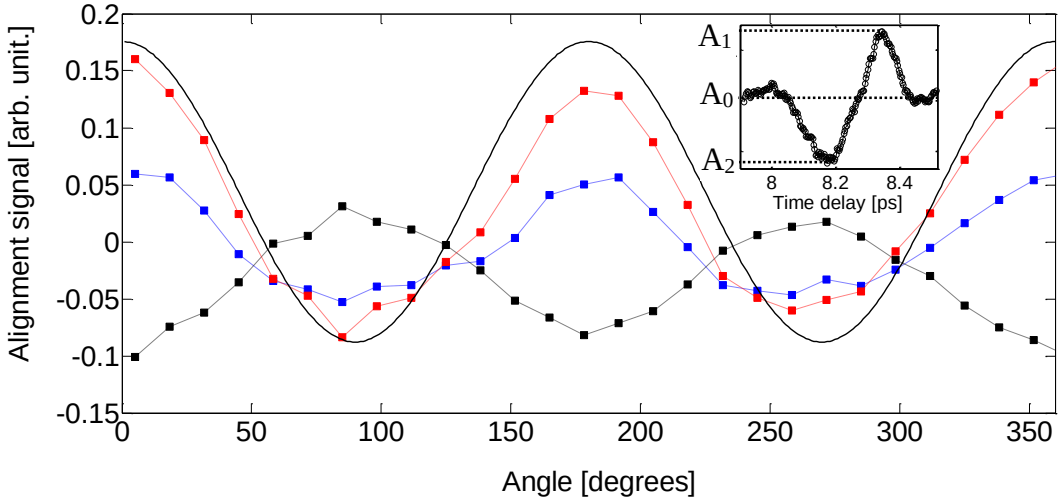

Figure 5.11 The variations of A_1 - A_0 (blue square), A_2 - A_0 (black square), and A_1 - A_2 (red square) as a function of α which is the angle between the pump and probe field directions around full revival for N_2, where A_1, A_0, and A_2 are determined as shown in the inset, and the solid line stands for the variation of A_1-A_2 which is calculated for the same conditions used in the experiment. The pump and probe peak intensities are $2x10^{13}W/cm^2$ and $5x10^{13}W/cm^2$, respectively.

In Figure 5.11 we plotted the modulation amplitude A_1 - A_0, A_2 - A_0, and A_1 - A_2, where A_1, A_0, and A_2 are the white-light signals measured at the alignment, at the random molecular orientations (no alignment), and at the anti-alignment, respectively, as shown in the inset of Figure 5.11. The modulation A_1 - A_2 reaches maxima for $\alpha = 0^\circ$, 180°, and 360° and reaches minima for $\alpha = 90^\circ$ and 270°. Here, we can conclude that the α-dependent modulation shows the white-light radiation is enhanced at the alignment where molecules are parallel to the probe pulse field polarization and

suppressed at the anti-alignment where molecules are perpendicular to the probe pulse field polarization. As follows from Figure 5.10 and Figure 5.11, the modulation phase is reversed at $\alpha_c \approx 55°$, where the white-light signal is independent of the time delay. We note that the existence of angle α_c, where the white-light signal is independent of the time delay, is a specific signature for the σ_g symmetry of the active molecular orbitals of N_2 [47].

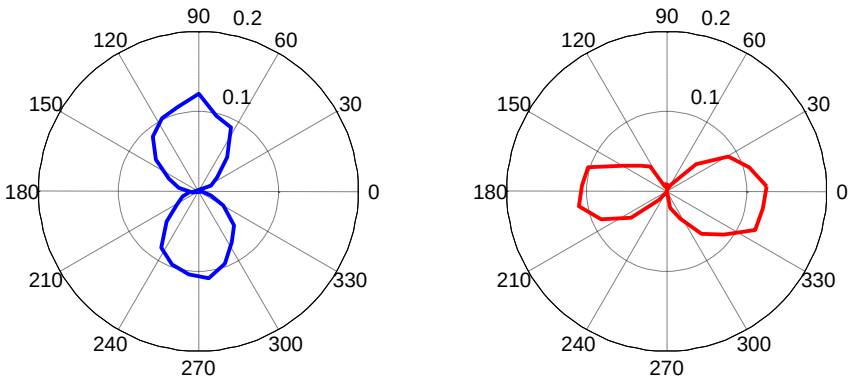

8.15ps 8.35ps

Figure. 5.12 The polar plots show alignment signals at delay times within the full revival as functions of the relative angle between pump and probe polarizations. Molecules are maximally anti-aligned (blue, showing negative change of the signal) around 8.15ps for $\alpha = 90^{\circ}, 270^{\circ}$ and aligned around 8.35 ps (red, showing positive change of the signal) for $\alpha = 0^{\circ}, 180^{\circ}$.

A polar plot presented in Figure. 5.12 shows how the molecular alignment changes at the maximal alignment delay (8.35ps) and anti-alignment delay (8.15ps) as the angle of the polarization of the pump pulse varied in experiment in respect to the polarization angle of the probe pulse that was fixed. The molecules are maximally anti-aligned along the polarization of the probe pulse for $\alpha = 90^{\circ}, 270^{\circ}$ simultaneously with the expected decrease of the refractive index around 8.15 ps, and they are maximally aligned along the polarization of the probe pulse for $\alpha = 0^{\circ}, 180^{\circ}$ where the refractive index increases around 8.35 ps.

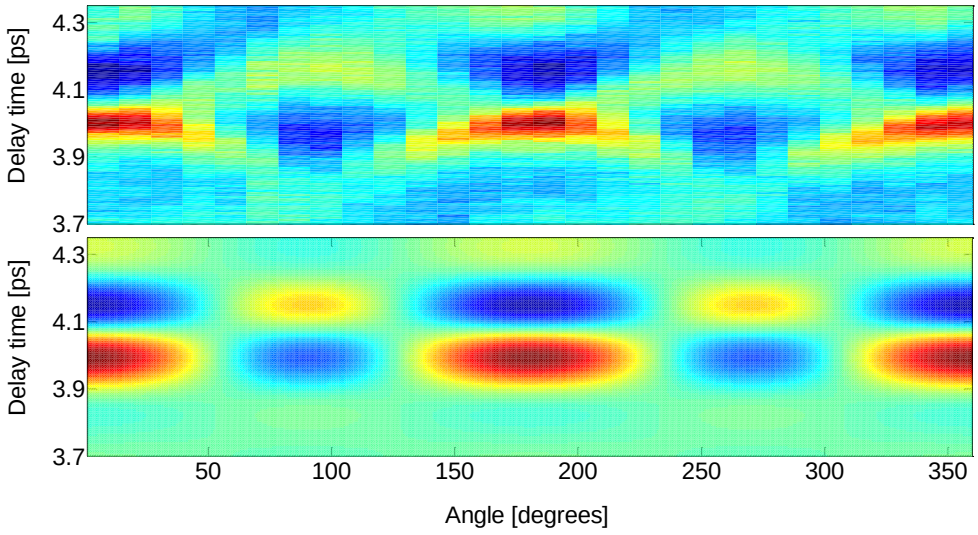

Figure 5.13 Experimental (top) and theoretical (bottom) quantum carpets of a rotational half revival around 4.1ps.

The series of plots presented in Figure 5.13 and Figure 5.15 shows similar results of rotational half revival and first quarter revival, respectively. For the half rotational revival, the molecules are aligned along the polarization of the probe pulse where the refractive index increases around 4 ps, and they are aligned perpendicular to this direction with a decrease of the refractive index around 4.15 ps as seen in Figure 5.14. However, at the half revival, the change of the alignment expectation comes with the opposite sign compared to the full revival.

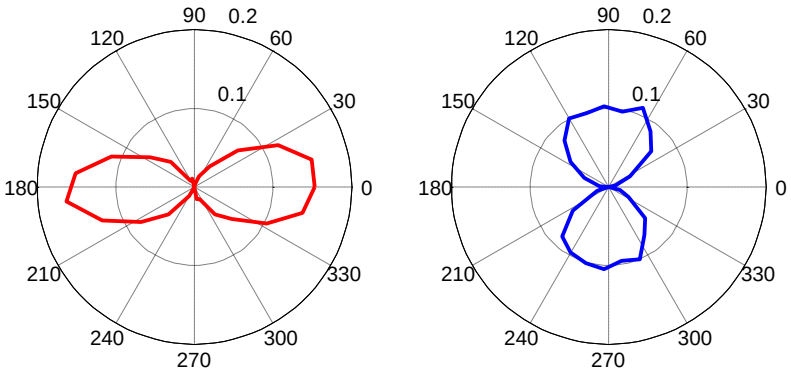

4 ps 4.15 ps

Figure 5.14 The polar plots show alignment signals at delay times within the half revival as functions of the relative angle between pump and probe polarizations. Molecules are maximally aligned (red) around 4 ps for $\alpha = 0^{\circ}, 180^{\circ}$ and anti-aligned (blue) around 4.15ps for $\alpha = 90^{\circ}, 270^{\circ}$.

At quarter revival the phase in the rotational wave packet depends on the parity of *J* state. The even and odd states have their phases shifted by π, and therefore they interfere destructively. The relative ratio of the statistical weights of even-N_2 versus odd-N_2 states is 2:1. Because of this 2:1 ratio for even/odd states, their contributions do not cancel completely each other, however, the signal has a reduced amplitude in comparison to the signal at the full and half revivals, as is also observed in the experiment (Figure 5.15).

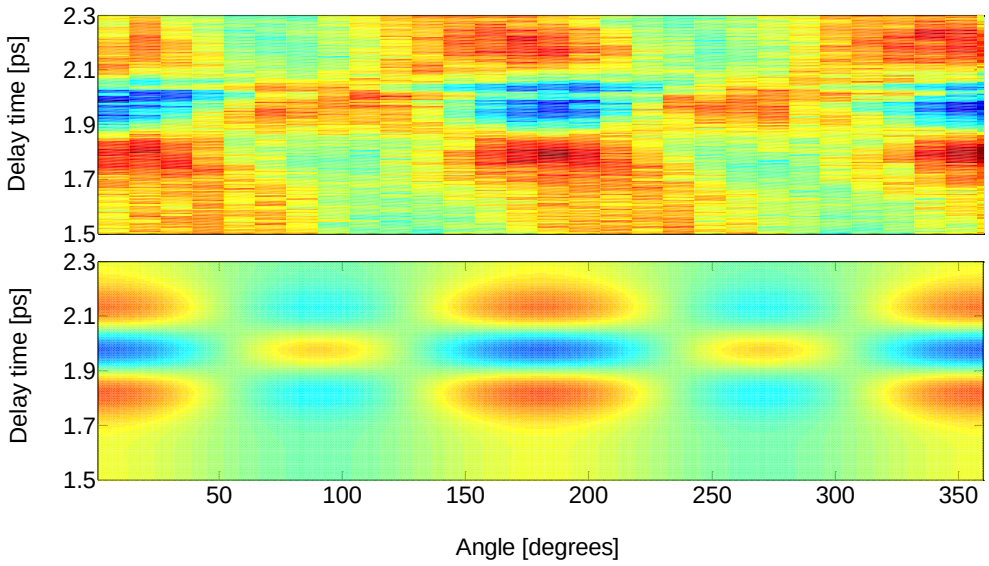

Figure 5.15 Experiment (top) and theory (bottom) of a rotational quarter revival around 2 ps.

The series of polar plots presented in Figure 5.16 shows how the molecular alignment changes with respect to the variable angle of the pump pulse around the first quarter revival. Due to the opposite contributions of the even and odd states they partially cancel each other, and therefore the molecular alignment signal is partially reduced compared to the full and half revivals. The molecules are maximally aligned along the polarization of the probe pulse with the simultaneous increase of the refractive index around 1.8 ps and 2.2ps for $\alpha = 0^{\circ}, 180^{\circ}$, and maximally anti-aligned with a decrease of the refractive index around 2 ps for $\alpha = 90^{\circ}, 270^{\circ}$.

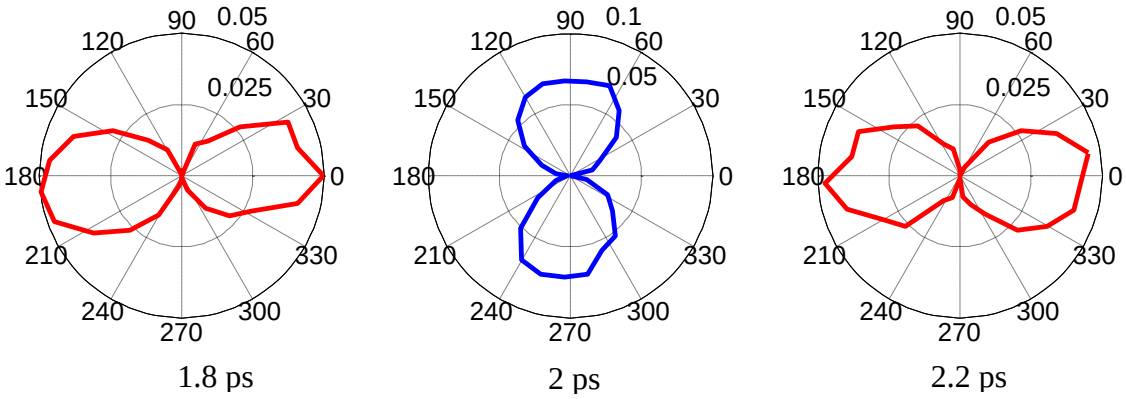

Figure 5.16 The polar plots show alignment signals within the first quarter revival. Molecules are aligned (red) around 1.8 ps and 2.2 ps for $\alpha = 0^{\circ}, 180^{\circ}$ and anti-aligned (blue) around 2.0ps for $\alpha = 90^{\circ}, 270^{\circ}$.

5.6 Conclusions

As an effective approach with a simple set-up based on the interaction between a filament-forming probe pulse and molecules pre-aligned by a pump pulse we implemented an experimental method to study field-free molecular alignment dynamics of nitrogen. The variations of the white-light generation were explained by the induced intensity-dependent variations of the refractive index. Theoretical calculations of nonadiabatic alignment agreed well with experimentally measured signals of white-light generation. Both results have shown agreement in the periods, shape and magnitude of the revival signals at full, half and quarter revivals of N_2. The measurements and calculated results of molecular alignment were matched within the temporal error of the experimental conditions. In addition, we mapped ultrafast rotational wave packets as a function of the delay and polarization angle between the pump and probe pulses (i.e. experimentally obtained "quantum carpet") by using femtosecond white-light generation from filaments to directly reconstruct the molecular alignment revivals in nitrogen. The experimental results of mapping rotational wave packets were also compared with quantum mechanical calculations and the results indicate that the calculations describe all major experimentally observed features.

CHAPTER VI

OVERALL CONCLUSIONS AND FUTURE PERSPECTIVES

We proposed and investigated an alternative approach for the molecular alignment monitoring based on measurement of photoelectrons produced by a delayed femtosecond probe beam. The photoelectron yields created from aligned molecules by linearly and circularly polarized pump pulses as a function of the linearly polarized probe pulse delay were used to observe the molecular revival events of N_2, O_2, CO_2, CO, and C_2H_2 gases. We also compared theoretical calculations of nonadiabatic alignment with experimental measurements. Additionally, by fitting the alignment theoretical model to measured data, we were able to obtain the rotational constants of these molecules observed for a linearly polarized pump pulse at field-free alignment condition. The rotational constants are in good agreement with the theoretical values. We show that creating and controlling molecular alignment with circular polarized laser pulses give us a new ability of field-free alignment of molecules outside of the polarization plane. We used the photoelectron measurement to study the alignment features but this technique can be used any specific probing method such as high harmonic generation, extreme ultraviolet transient absorption, or ultrafast x-ray diffraction with higher density gas sources [13,125,126].

When a filamenting probe pulse propagates through the molecules aligned by preceding pump pulse, it experiences a spatial refractive index variation and changes its spatial intensity distribution. This spatial variation is related with the degree of molecular alignment and can be used to reconstruct revivals of the molecular alignment. Therefore,

we implemented experimental method to study field-free molecular alignment dynamics of nitrogen based on the interaction between filament and pre-aligned molecules. We mapped ultrafast rotational wave packets (quantum carpet) as a function of the delay and polarization angle between the pump and probe pulses by using femtosecond white-light generation from filaments to directly reconstruct the molecular alignment revivals in nitrogen. Beyond understanding the dynamics of molecules interacting with ultrafast laser pulses, this idea can be applied to any process related with the molecular alignment. The results of the quantum carpet show that an ensemble of molecules at room temperature can be arranged into an ordered state by molecular alignment which provides fine spectroscopic accuracy. Besides, the technique of using a filament as a probe for molecular alignment we purposed is easy to implement in a typical ultrafast laser facility, it represents an important step to extend the experimental interest in other gases and also more complex systems, such as the organic molecules and for much shorter time scales, such as given by attosecond laser pulses. In addition we directly measured the variations of the femtosecond pulse duration that interacted with the aligned N_2 molecules, which can be used for tailoring laser pulses and their filamentation.

REFERENCES

[1] J.H. Posthumus, Reports on Progress in Physics 67 (2004) 623.

[2] A. Becker, F.H.M. Faisal, Journal of Physics B: Atomic, Molecular and Optical Physics 38 (2005) R1.

[3] P. Agostini, F. Fabre, G. Mainfray, G. Petite, R.N. K., Phys. Rev. Lett. 42 (1979) 1127.

[4] J. Levesque, P.B. Corkum, Canadian Journal of Physics 84 (2006) 1.

[5] P.B. Corkum, a.F. Krausz, Nat. Phys. 3 (2007) 381

[6] X.F. Li, A. L'Huillier, M. Ferray, L.A. Lompré, G. Mainfray, Physical Review A 39 (1989) 5751.

[7] R.S. Judson, H. Rabitz, Physical Review Letters 68 (1992) 1500.

[8] A.H. Zewail, The Journal of Physical Chemistry A 104 (2000) 5660.

[9] H. Stapelfeldt, T. Seideman, Reviews of Modern Physics 75 (2003) 543.

[10] T. Seideman, E. Hamilton, in: P.R. Berman, C.C. Lin (Eds.), Advances In Atomic, Molecular, and Optical Physics, Academic Press, 2005, p. 289.

[11] S. Henrik, Physica Scripta 2004 (2004) 132.

[12] S. Fleischer, I.S. Averbukh, Y. Prior, Physical Review A 74 (2006) 041403.

[13] J. Itatani, J. Levesque, D. Zeidler, H. Niikura, H. Pepin, J.C. Kieffer, P.B. Corkum, D.M. Villeneuve, Nature 432 (2004) 867.

[14] C. Vozzi, F. Calegari, E. Benedetti, J.P. Caumes, G. Sansone, S. Stagira, M. Nisoli, R. Torres, E. Heesel, N. Kajumba, J.P. Marangos, C. Altucci, R. Velotta, Physical Review Letters 95 (2005) 153902.

[15] M. Meckel, D. Comtois, D. Zeidler, A. Staudte, D. Pavičić, H.C. Bandulet, H. Pépin, J.C. Kieffer, R. Dörner, D.M. Villeneuve, P.B. Corkum, Science 320 (2008) 1478.

[16] C.Z. Bisgaard, O.J. Clarkin, G. Wu, A.M.D. Lee, O. Geßner, C.C. Hayden, A. Stolow, Science 323 (2009) 1464.

[17] L. Holmegaard, J.L. Hansen, L. Kalhoj, S. Louise Kragh, H. Stapelfeldt, F. Filsinger, J. Kupper, G. Meijer, D. Dimitrovski, M. Abu-samha, C.P.J. Martiny, L. Bojer Madsen, Nat Phys 6 (2010) 428.

[18] J.L. Hansen, H. Stapelfeldt, D. Dimitrovski, M. Abu-samha, C.P.J. Martiny, L.B. Madsen, Physical Review Letters 106 (2011) 073001.

[19] E. Gershnabel, I.S. Averbukh, Physical Review Letters 104 (2010) 153001.

[20] R.J. Gordon, L. Zhu, W.A. Schroeder, T. Seideman, Journal of Applied Physics 94 (2003) 669.

[21] R.A. Bartels, T.C. Weinacht, N. Wagner, M. Baertschy, C.H. Greene, M.M. Murnane, H.C. Kapteyn, Physical Review Letters 88 (2001) 013903.

[22] K.F. Lee, D.M. Villeneuve, P.B. Corkum, E.A. Shapiro, Physical Review Letters 93 (2004) 233601.

[23] F. Calegari, C. Vozzi, S. Gasilov, E. Benedetti, G. Sansone, M. Nisoli, S. De Silvestri, S. Stagira, Physical Review Letters 100 (2008) 123006.

[24] J. Wu, H. Cai, H. Zeng, A. Couairon, Opt. Lett. 33 (2008) 2593.

[25] J. Wu, H. Cai, Y. Peng, Y. Tong, A. Couairon, H. Zeng, Laser Phys. 19 (2009) 1759.

[26] H. Cai, J. Wu, Y. Peng, H. Zeng, Opt. Express 17 (2009) 5822.

[27] F. Calegari, C. Vozzi, S. Stagira, Physical Review A 79 (2009) 023827.

[28] Y. Wang, X. Dai, J. Wu, L.e. Ding, H. Zeng, Applied Physics Letters 96 (2010) 031105.

[29] S. Varma, Y.H. Chen, J.P. Palastro, A.B. Fallahkair, E.W. Rosenthal, T. Antonsen, H.M. Milchberg, Physical Review A 86 (2012) 023850.

[30] V. Loriot, E. Hertz, B. Lavorel, O. Faucher, Journal of Physics B: Atomic, Molecular and Optical Physics 41 (2008) 015604.

[31] D. Pavičić, K.F. Lee, D.M. Rayner, P.B. Corkum, D.M. Villeneuve, Physical Review Letters 98 (2007) 243001.

[32] I.V. Litvinyuk, K.F. Lee, P.W. Dooley, D.M. Rayner, D.M. Villeneuve, P.B. Corkum, Physical Review Letters 90 (2003) 233003.

[33] E. Péronne, M.D. Poulsen, C.Z. Bisgaard, H. Stapelfeldt, T. Seideman, Physical Review Letters 91 (2003) 043003.

[34] M. Kenzo, S. Takayuki, N. Didier, Journal of Physics B: Atomic, Molecular and Optical Physics 37 (2004) 753.

[35] I. Nevo, L. Holmegaard, J.H. Nielsen, J.L. Hansen, H. Stapelfeldt, F. Filsinger, G. Meijer, J. Kupper, Physical Chemistry Chemical Physics 11 (2009) 9912.

[36] P.W. Dooley, I.V. Litvinyuk, K.F. Lee, D.M. Rayner, M. Spanner, D.M. Villeneuve, P.B. Corkum, Physical Review A 68 (2003) 023406.

[37] R. Velotta, N. Hay, M.B. Mason, M. Castillejo, J.P. Marangos, Physical Review Letters 87 (2001) 183901.

[38] N. Hay, R. Velotta, M. Lein, R. de Nalda, E. Heesel, M. Castillejo, J.P. Marangos, Physical Review A 65 (2002) 053805.

[39] T. Kanai, S. Minemoto, H. Sakai, Nature 435 (2005) 470.

[40] J.P. Marangos, S. Baker, N. Kajumba, J.S. Robinson, J.W.G. Tisch, R. Torres, Physical Chemistry Chemical Physics 10 (2008) 35.

[41] N. Kajumba, R. Torres, G.U. Jonathan, J.S. Robinson, S. Baker, J.W.G. Tisch, R.d. Nalda, W.A. Bryan, R. Velotta, C. Altucci, I. Procino, I.C.E. Turcu, J.P. Marangos, New Journal of Physics 10 (2008) 025008.

[42] C.B. Madsen, A.S. Mouritzen, T.K. Kjeldsen, L.B. Madsen, Physical Review A 76 (2007) 035401.

[43] D. Shafir, Y. Mairesse, D.M. Villeneuve, P.B. Corkum, N. Dudovich, Nat Phys 5 (2009) 412.

[44] B.K. McFarland, J.P. Farrell, P.H. Bucksbaum, M. Gühr, Science 322 (2008) 1232.

[45] C.T.L. Smeenk, P.B. Corkum, Journal of Physics B: Atomic, Molecular and Optical Physics 46 (2013) 201001.

[46] X. Xie, K. Doblhoff-Dier, H. Xu, S. Roither, M.S. Schöffler, D. Kartashov, S. Erattupuzha, T. Rathje, G.G. Paulus, K. Yamanouchi, A. Baltuška, S. Gräfe, M. Kitzler, Physical Review Letters 112 (2014) 163003.

[47] A. Abdurrouf, F.H.M. Faisal, Physical Review A 79 (2009) 023405.

[48] R. Torres, N. Kajumba, J.G. Underwood, J.S. Robinson, S. Baker, J.W.G. Tisch, R. de Nalda, W.A. Bryan, R. Velotta, C. Altucci, I.C.E. Turcu, J.P. Marangos, Physical Review Letters 98 (2007) 203007.

[49] K. Miyazaki, M. Kaku, G. Miyaji, A. Abdurrouf, F.H.M. Faisal, Physical Review Letters 95 (2005) 243903.

[50] N. Berti, P. Béjot, J.P. Wolf, O. Faucher, Physical Review A 90 (2014) 053851.

[51] W. Schippers, E. Gershnabel, J. Burgmeier, O. Katz, U. Willer, I.S. Averbukh, Y. Silberberg, W. Schade, Appl. Phys. B 105 (2011) 203.

[52] S.K. Lee, Y.F. Lin, L. Yan, W. Li, The Journal of Physical Chemistry A 116 (2012) 1950.

[53] Z. Hu, X. Lai, X. Liu, J. Chen, Physical Review A 89 (2014) 043401.

[54] C.T.L. Smeenk, L. Arissian, A.V. Sokolov, M. Spanner, K.F. Lee, A. Staudte, D.M. Villeneuve, P.B. Corkum, Physical Review Letters 112 (2014) 253001.

[55] N. Xu, J. Li, J. Li, Z. Zhang, Q. Fan, in: K. Jakubczak (Ed.), Lasers - Applications in Science and Industry, 2011.

[56] I.S. Averbukh, N.F. Perelman, Physics Letters A 139 (1989) 449.

[57] R.W. Robinett, Physics Reports 392 (2004) 1.

[58] G.H. Lee, H.T. Kim, J.Y. Park, C.H. Nam, T.K. Kim, J.H. Lee, H. Ihee, Journal of the Korean Physical Society 49 (2006) 337.

[59] B. Friedrich, D. Herschbach, Physical Review Letters 74 (1995) 4623.

[60] B.J. Sussman, J.G. Underwood, R. Lausten, M.Y. Ivanov, A. Stolow, Physical Review A 73 (2006) 053403.

[61] B.W. Shore, The Theory of Coherent Atomic Excitation, Multilevel Atoms and Incoherence, Wiley, 1990.

[62] T. Seideman, The Journal of Chemical Physics 107 (1997) 10420.

[63] J.D. Graybeal, Molecular spectroscopy, McGraw-Hill, 1988.

[64] S.M. Purcell, P.F. Barker, Physical Review Letters 103 (2009) 153001.

[65] S.M. Purcell, UCL (University College London), 2010.

[66] S.M. Purcell, P.F. Barker, Physical Review A 82 (2010) 033433.

[67] F.H.M. Faisal, A. Abdurrouf, Physical Review Letters 100 (2008) 123005.

[68] B. Friedrich, Herschbach, The Journal of Physical Chemistry A 103 (1999) 10280.

[69] B. Friedrich, D. Herschbach, The Journal of Chemical Physics 111 (1999) 6157.

[70] J. Ortigoso, M. Rodríguez, M. Gupta, B. Friedrich, The Journal of Chemical Physics 110 (1999) 3870.

[71] P.F. Bernath, P.F. Bernath, Spectra of Atoms and Molecules, Oxford University Press, New York, 1995.

[72] H. Stapelfeldt, T. Seideman, Reviews of Modern Physics 75 (2003) 543.

[73] A. Ben Haj-Yedder, A. Auger, C.M. Dion, E. Cancès, A. Keller, C. Le Bris, O. Atabek, Physical Review A 66 (2002) 063401.

[74] E. Hamilton, T. Seideman, T. Ejdrup, M.D. Poulsen, C.Z. Bisgaard, S.S. Viftrup, H. Stapelfeldt, Physical Review A 72 (2005) 043402.

[75] D.A. Varshalovich, A.N. Moskalev, V.K. Khersonskiĭ, Quantum Theory of Angular Momentum: Irreducible Tensors, Spherical Harmonics, Vector Coupling Coefficients, 3nj Symbols, World Scientific Pub., 1988.

[76] R.N. Zare, Angular momentum: understanding spatial aspects in chemistry and physics, Wiley, 1988.

[77] B.H. Bransden, C.J. Joachain, Physics of Atoms and Molecules, Prentice Hall, 2003.

[78] D.A. McQuarrie, J.D. Simon, Physical Chemistry: A Molecular Approach, University Science Books, 1997.

[79] M. Machholm, The Journal of Chemical Physics 115 (2001) 10724.

[80] J.-C. Diels, W. Rudolph, Ultrashort laser pulse phenomena, Academic press, 2006.

[81] R. Trebino, K.W. DeLong, D.N. Fittinghoff, J.N. Sweetser, M.A. Krumbügel, B.A. Richman, D.J. Kane, Review of Scientific Instruments 68 (1997) 3277.

[82] http://www.swampoptics.com/tutorials_autocorrelation.htm, http://www.swampoptics.com/tutorials_GRENOUILLE.htm.

[83] M. Protopapas, C.H. Keitel, P.L. Knight, Reports on Progress in Physics 60 (1997) 389.

[84] S.P. Vladimir, Physics-Uspekhi 47 (2004) 855.

[85] P. Atkins, J. de Paula, R. Friedman, Quanta, Matter, and Change: A Molecular Approach to Physical Chemistry, OUP Oxford, 2009.

[86] F.H.M. Faisal, A. Abdurrouf, K. Miyazaki, G. Miyaji, Physical Review Letters 98 (2007) 143001.

[87] H. Li, W. Li, Y. Feng, J. Liu, H. Pan, H. Zeng, Physical Review A 85 (2012) 052515.

[88] G.A. West, J.J. Barrett, Optics Letters 4 (1979) 395.

[89] R.B. Philip, J. Per, Molecular Symmetry and Spectroscopy, 2nd Ed, NRC Research Press, 2006.

[90] W.M.L.D.R. Haynes, CRC handbook of chemistry and physics : a ready-reference book of chemical and physical data, CRC Press, Boca Raton, Fla., 2011.

[91] M. Herman, A. Campargue, M.I. El Idrissi, J. Vander Auwera, Journal of Physical and Chemical Reference Data 32 (2003) 921.

[92] D.S. Steingrube, E. Schulz, T. Binhammer, M.B. Gaarde, A. Couairon, U. Morgner, M. Kovačev, New Journal of Physics 13 (2011) 043022.

[93] M. Rodriguez, R. Bourayou, G. Méjean, J. Kasparian, J. Yu, E. Salmon, A. Scholz, B. Stecklum, J. Eislöffel, U. Laux, A.P. Hatzes, R. Sauerbrey, L. Wöste, J.-P. Wolf, Physical Review E 69 (2004) 036607.

[94] C.P. Hauri, W. Kornelis, F.W. Helbing, A. Heinrich, A. Couairon, A. Mysyrowicz, J. Biegert, U. Keller, Appl. Phys. B 79 (2004) 673.

[95] S. Skupin, G. Stibenz, L. Bergé, F. Lederer, T. Sokollik, M. Schnürer, N. Zhavoronkov, G. Steinmeyer, Physical Review E 74 (2006) 056604.

[96] S. Varma, Y.H. Chen, H.M. Milchberg, Physical Review Letters 101 (2008) 205001.

[97] A. Couairon, A. Mysyrowicz, Physics Reports 441 (2007) 47.

[98] Y.H. Chen, S. Varma, H.M. Milchberg, J. Opt. Soc. Am. B 25 (2008) B122.

[99] J.-F. Ripoche, G. Grillon, B. Prade, M. Franco, E. Nibbering, R. Lange, A. Mysyrowicz, Optics Communications 135 (1997) 310.

[100] S. Varma, Y.-H. Chen, H.M. Milchberg, Physics of Plasmas (1994-present) 16 (2009) 056702.

[101] Y. Feng, H. Pan, J. Liu, C. Chen, J. Wu, H. Zeng, Opt. Express 19 (2011) 2852.

[102] J. Kasparian, M. Rodriguez, G. Méjean, J. Yu, E. Salmon, H. Wille, R. Bourayou, S. Frey, Y.-B. André, A. Mysyrowicz, R. Sauerbrey, J.-P. Wolf, L. Wöste, Science 301 (2003) 61.

[103] C. D'Amico, A. Houard, M. Franco, B. Prade, A. Mysyrowicz, A. Couairon, V.T. Tikhonchuk, Physical Review Letters 98 (2007) 235002.

[104] M. Durand, K. Lim, V. Jukna, E. McKee, M. Baudelet, A. Houard, M. Richardson, A. Mysyrowicz, A. Couairon, Physical Review A 87 (2013) 043820.

[105] F. Krausz, M. Ivanov, Reviews of Modern Physics 81 (2009) 163.

[106] E. Goulielmakis, M. Schultze, M. Hofstetter, V.S. Yakovlev, J. Gagnon, M. Uiberacker, A.L. Aquila, E.M. Gullikson, D.T. Attwood, R. Kienberger, F. Krausz, U. Kleineberg, Science 320 (2008) 1614.

[107] W.A. Bryan, E.M.L. English, J. McKenna, J. Wood, C.R. Calvert, I.C.E. Turcu, R. Torres, J.L. Collier, I.D. Williams, W.R. Newell, Physical Review A 76 (2007) 023414.

[108] M. Leibscher, B. Schmidt, Physical Review A 80 (2009) 012510.

[109] J.H. Marburger, Prog. Quantum Electron. 4 (1975) 35.

[110] S.L. Chin, Femtosecond Laser Filamentation, Springer, New York, 2010.

[111] M. Kolesik, G. Katona, J.V. Moloney, E.M. Wright, Physical Review Letters 91 (2003) 043905.

[112] F. DeMartini, C.H. Townes, T.K. Gustafson, P.L. Kelley, Physical Review 164 (1967) 312.

[113] Y.H. Chen, S. Varma, A. York, H.M. Milchberg, Opt. Express 15 (2007) 11341.

[114] M.Z. Hoque, M. Lapert, E. Hertz, F. Billard, D. Sugny, B. Lavorel, O. Faucher, Physical Review A 84 (2011) 013409.

[115] J. Houzet, F. Billard, E. Hertz, D. Chateau, F. Chaussard, B. Lavorel, O. Faucher, Appl. Phys. B 108 (2012) 897.

[116] E. Hertz, D. Daems, S. Guérin, H.R. Jauslin, B. Lavorel, O. Faucher, Physical Review A 76 (2007) 043423.

[117] J.K. Wahlstrand, H.M. Milchberg, Opt. Lett. 36 (2011) 3822.

[118] J.H. Odhner, D.A. Romanov, E.T. McCole, J.K. Wahlstrand, H.M. Milchberg, R.J. Levis, Physical Review Letters 109 (2012) 065003.

[119] S. Yuan, M. Li, Y. Feng, H. Li, L. Zheng, S.L. Chin, H. Zeng, Journal of Physics B: Atomic, Molecular and Optical Physics 48 (2015) 094018.

[120] C. Marceau, S. Ramakrishna, S. Génier, T.-J. Wang, Y. Chen, F. Théberge, M. Châteauneuf, J. Dubois, T. Seideman, S.L. Chin, Optics Communications 283 (2010) 2732.

[121] R.W. Boyd, in: R.W. Boyd (Ed.), Nonlinear Optics (Third Edition), Academic Press, Burlington, 2008, p. 329.

[122] P. Béjot, Y. Petit, L. Bonacina, J. Kasparian, M. Moret, J.P. Wolf, Opt. Express 16 (2008) 7564.

[123] G.P. Agrawal, in: G.P. Agrawal (Ed.), Nonlinear Fiber Optics (Fourth Edition), Academic Press, San Diego, 2006, p. 226.

[124] S.L. Chin, S.A. Hosseini, W. Liu, Q. Luo, F. Théberge, N. Aközbek, A. Becker, V.P. Kandidov, O.G. Kosareva, H. Schroeder, Canadian Journal of Physics 83 (2005) 863.

[125] E. Goulielmakis, Z.-H. Loh, A. Wirth, R. Santra, N. Rohringer, V.S. Yakovlev, S. Zherebtsov, T. Pfeifer, A.M. Azzeer, M.F. Kling, S.R. Leone, F. Krausz, Nature 466 (2010) 739.

[126] F. Filsinger, G. Meijer, H. Stapelfeldt, H.N. Chapman, J. Kupper, Physical Chemistry Chemical Physics 13 (2011) 2076.